FootHack: An Untethered Shoe Prototype for Hacking Feet with Pneumatic and Vibrotactile Feedback

MARCO TORGE GABRECHT✉, Technical University of Applied Sciences Lübeck, Germany and Fraunhofer IMTE, Germany
HANS-CHRISTIAN JETTER, University of Luebeck, Germany
DENYS J.C. MATTHIES, Technical University of Applied Sciences Lübeck, Germany and Fraunhofer IMTE, Germany

This paper taps into the intricate relationship between the manipulation of haptic feedback under the foot while walking and its resulting impact on our physio-psychological perception. To investigate this, we developed an untethered 3D-printed shoe prototype that provides pneumatic and vibrotactile feedback. In this paper, we share our engineering efforts and findings to replicate our prototype. We conducted three experiments, the first of which, involving 9 participants, found that the perception of haptic feedback under the foot is comparatively slower and less sensitive, while, audio noise surprisingly also has a significant influence. In a second study, we show with 3 pilot participants and 9 participants how to manipulate the user's gait. We demonstrate how to impact the stance time and observe a small baseline-corrected directional bias below one degree on average over 10 m. In our final and third study, we use the prototype to simulate five different terrains in a virtual environment. The realism of this illusion was rated fairly good by 20 users scoring 7.17 on an 11-point Likert scale.

CCS Concepts: • **Human-centered computing** → *Haptic devices.*

Additional Key Words and Phrases: Smart Shoe, Wearable Computing, Prototyping, Vibrotactile Feedback, Pneumatic, Illusive Feedback, Perception Studies, Empiric Evaluation

ACM Reference Format:
Marco Torge Gabrecht, Hans-Christian Jetter, and Denys J.C. Matthies. 2026. FootHack: An Untethered Shoe Prototype for Hacking Feet with Pneumatic and Vibrotactile Feedback. *Proc. ACM Interact. Mob. Wearable Ubiquitous Technol.* 10, 4, Article 215 (December 2026), 29 pages. https://doi.org/10.1145/3857990

1 Introduction

The foot, endowed with a higher density of sensor cells than the human face [41], presents a unique platform for haptic interaction due to its high resolution for haptic perception [17]. The plantar skin contains Merkel cells and Ruffini endings that respond to sustained pressure and skin stretch, as well as Meissner and Pacinian corpuscles that respond to light touch and vibration. Together with proprioception, these receptors contribute to balance, gait control, and the perception of the ground. It is surprising that wearable foot interfaces are yet to prevail [2]. Only a few products have managed to penetrate the market [47, 73, 74], focusing primarily on applications such as running quantification and gaming experience enhancement [33]. This scarcity is mirrored in the academic realm, where augmented foot interfaces predominantly center around input sensing [21].

Authors' Contact Information: Marco Torge Gabrecht (corresponding author), Technical University of Applied Sciences Lübeck, Lübeck, Germany and Fraunhofer IMTE, Lübeck, Germany, marco.gabrecht@th-luebeck.de; Hans-Christian Jetter, University of Luebeck, Institute of Multimedia and Interactive Systems, Luebeck, Germany, hanschristian.jetter@uni-luebeck.de; Denys J.C. Matthies, Technical University of Applied Sciences Lübeck, Lübeck, Germany and Fraunhofer IMTE, Lübeck, Germany, denys.matthies@th-luebeck.de.



This work is licensed under a Creative Commons Attribution 4.0 International License.
© 2026 Copyright held by the owner/author(s).
ACM 2474-9567/2026/12-ART215
https://doi.org/10.1145/3857990



Fig. 1. Depicting the prototype: a) Top view of the insole with coin vibration motors, b) Backside of the midsole, c) Assembled prototype showing the shoe with the outersole (back side). In summary, the prototype consists of an IMU, Pressure Sensors, Solenoid Valves, Coin Vibrators, a Battery, Antenna, and a custom PCB, which houses the ESP32 and MOSFET Stages etc. d) The cross-section of the CAD-Design. On the left, we can see the midsole. Colored in slight blue: inner shell, yellow: Chambers with stabilisation stages, the blue 1 marks the front chamber and blue 2 marks the heel chamber, gray is space for components. Red 1 and 4 are air outtake valves, red 2 and 3 are the connection valves between the chambers. Green 1 and 2 are the pressure sensors, brown 1 is the space for the PCB and battery stacked on top. Above the green 1, a small dark line shows the external antenna space. To the right, the insole features holes for the coin-cell vibration motors.

FootHack does not introduce a new actuator principle. Its technical contribution is the integration of pneumatic and vibrotactile actuation, gait-driven pressure accumulation, pressure-based gait-event sensing, and untethered electronics within one insole. To match future standards, we found it particularly important to develop a prototype that employs a practical and seamless aesthetic device to ensure that users experience the least possible disruption and hindrance while performing their tasks. Besides our engineering contribution, we aim to understand our deployed haptic feedback and to ultimately "hack feet". For this, our research is guided by three research questions:

RQ1: What are the reaction properties when deploying vibration and pneumatic feedback under the foot? With nine participants, we ran a reaction test comparing eye-to-hand and foot-to-hand reactions under three different noise levels (silence, soothing music, loud noise). We found that noise affected the perception of tactile feedback at the feet, which is slower and less sensitive than optical stimulation.

RQ2: How can we manipulate the user's walking physiology by applying haptic feedback under the foot? In a pilot with three participants, we initially tested four conditions: no vibration, random vibration, full vibration, and vibration mapped to the center of pressure, evidencing an enlarged stance time during actuation. Subsequently, with nine participants, we evaluated vibration and cushioning across nine conditions and observed a small baseline-corrected association between asymmetric feedback and walking direction under restricted visual and auditory correction.

RQ3: How can we create the illusion of different terrains to enrich virtual reality environments? Finally, we evaluated five simulated terrains, each rendered with combined pneumatic and vibrotactile feedback, with 20 participants in VR. The pressure-regulated Linoleum condition served as the hard-surface reference. Across all conditions, perceived realism averaged 7.17 on an 11-point scale from 1 (not realistic) to 11 (fully realistic) [40].

Therefore, following Wobbrock's [87] taxonomy, our contributions fall into two categories: one *artifact contribution*: an untethered pneumatic and vibrotactile shoe prototype, and three *empirical contributions*: studies that investigate foot-based feedback for interaction. The artifact combines a fully insole-embedded architecture, gait-driven pressure accumulation, pressure-based gait-event sensing, and terrain rendering through regulated pressure or free inter-chamber exchange with terrain-specific vibration (Table 2). Archived raw-ADC traces

document pressure accumulation but not harvested energy. Quantifying the stored pneumatic energy would require pressure and chamber-volume-change measurements, which were not part of this study.

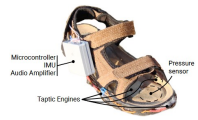
The studies follow a common progression: Study 1 examines whether underfoot cues are perceived, Study 2 tests whether gait and walking direction are affected, and Study 3 uses the same pneumatic and vibrotactile feedback to simulate terrain in VR. The studies do not evaluate a combined terrain-rendering and steering application.

2 Related Work

2.1 Sensing the Foot

For understanding human movement [28], biomechanics [61, 88], environmental factors [44, 91], and health considerations [5], literature has shown many types of sensors, including: IMUs, which capture three-dimensional motion characteristics [34, 42], Pressure Sensors, which measure ground contact and force distribution [22, 23, 51], Flexible Contact Vibration Sensors, to identify user activities and ground surfaces [80], Temperature and Humidity Sensors, which monitor diabetic foot health and detect ulceration conditions [49, 60], Strain Gauges, which

Table 1. Comparison of most related wearable haptic foot interfaces. *Untethered* means no cabled connections or offboard hardware are required for operation. *No added burden* means the system does not introduce substantial walking hindrance such as an elevated/plateau sole or excessive shoe mass; specific burdens (if any) are listed.

Prototype	Application	Actuation	No added burden	Untethered
 *RealWalk* [66]	Ground-material deformation in HMD-based VR (snow, mud, dry sand).	MR-fluid cylinders with current-controlled viscosity; insole pressure map drives deformation profiles.	Elevated/plateau due to bulky metal actuator modules; external tracking; device mass not reported.	✗
 *Smart Shoe* [83, 84]	Slopes and uneven terrain; treadmill/CAVE VR; gait training (incl. PD).	Multi-bladder pneumatics with selective valve actuation; passive elastomeric reinflation.	High mass (892–1120 g per shoe); thick/raised soft-robotic sole; treadmill + Vicon infra.	✗
 *VibeWalk* [3]	Navigation cues; sensorimotor rehabilitation; stance & walking tacton recognition.	Four LRAs at heel, toe, metatarsal heads; tactons time-locked to gait events.	✓	✓
 *bARefoot* [67]	Virtual material experiences; motion-coupled vibrotactile exploration.	Motion-coupled vibrotactile feedback mapping movement dynamics to vibration parameters.	✓	✓
 **FootHack**	VR/MR terrain illusions; gait manipulation via asymmetric, time-locked cues; extended mobile use.	Insole-integrated pneumatic chambers plus localized vibrotactile motors under ESP32 control.	✓	✓

measure stretch, bend, and pressure changes in wearable applications [12], Pedometers, which count steps and estimate distance [34], GPS, which tracks location, height differences, speed, and distance in real-world settings, Capacitive Sensors, which identify walking styles, foot gestures, and floor types [7, 31, 43], Infrared Sensors, which are also often used for stationary gait analysis [16, 18, 30], Microphones, which determine gait parameters based on the sound of footsteps [79, 79], and Cameras, which provide the most common visual approach to posture and gait analysis [8, 10, 82].

2.2 Actuating the Foot

Comparatively little research has exploited the foot's unique ability to perceive tactile stimuli for interaction purposes. Still, there is a number of actuators that have been explored for user feedback, including: Vibration motors, which produce vibrotactile sensation with different frequencies and amplitudes [19, 24, 42, 45, 58, 65, 78, 85, 89], Servomotors, which rotate or tilt a platform or a mechanism to change the orientation or shape of the shoe or insole [57], Solenoids, which generate a linear motion or a force when activated [82, 92], Shape-Memory-Alloys, which change their shape or size when heated by an electric current [39], Air chambers, which change the volume or pressure of air inside them [82, 84, 94], and other actuators, such as foot-tickling mechanisms [20], EMS [32], and Peltier Elements [43].

2.3 Manipulating Foot-Based Perception

Historically, the manipulation of foot-based perception has been touched upon in HCI research [1, 6, 57, 86], with works like Raihana et al. [57] attempting to simulate level ground walking on uneven surfaces, and Wang et al. [82] introducing dynamic terrain simulation through bladder-based shoe actuators. Subsequent studies [83, 84] simulated cobblestone terrains within a virtual environment. Further, Strohmeier et al. [67] developed a sandal-prototype with a vibrotactile actuator generating virtual material experiences such as compliance, elasticity, or friction for AR and VR purposes. Other related works include *FeetThrough* [76], which uses electrotactile stimulation to preserve real-world sensations, while *Level-Ups* [63] explores motorized stilts to simulate steps in VR. *FrictShoes* [75] provides multilevel friction feedback, and *Push-Ups* [81] uses shape-forming pneumatic devices for kinesthetic sensations. Another line of research addresses gait manipulation, for instance *Cruise Control for Pedestrians* [55], which relies on electrical muscle stimulation to guide walking direction. *DreamWalker* [90] enables continuous redirection while wearing a VR headset. *Gilded Gait* [71] superimposes vibrotactile illusions on footsteps, and galvanic vestibular stimulation has been shown to affect user balance and turning [35].

Delineation and Novelty. FootHack advances wearable foot haptics by combining controllable pneumatic compliance with localized vibrotactile cues in a single, fully integrated insole that operates without external hardware. Table 1 compares it with the most closely related wearable foot interfaces. Prior systems demonstrate valuable but partial capabilities: RealWalk produces material–like deformation through magnetorheological actuators but relies on bulky cylinder modules mounted between the base sole and the upper and on external tracking, which constrains free walking [66]. The Smart Shoe renders uneven terrain with a multi–bladder pneumatic sole but introduces substantial burden, with a per–shoe mass of approximately 0.9–1.1 kg and external electronics on the upper [83, 84]. VibeWalk establishes that foot–sole tactons are perceivable and useful for navigation and rehabilitation, although it restricts itself to vibrotactile messaging rather than multi–modal underfoot mechanics [3]. bARefoot demonstrates motion–coupled vibrotactile feedback for virtual material experiences, yet it remains limited to vibratory cues without compliance modulation [67].

Our design integrates the strengths of these approaches while addressing their critical limitations. Like the Smart Shoe, FootHack modulates sole compliance, but it does so in a compact insole architecture that embeds actuators, sensors, communication, and power directly within the insole volume, thereby preserving natural gait and avoiding the protruding plateau structures that have rendered earlier pneumatic systems heavy and

difficult to walk with [83, 84]. Like VibeWalk and bARefoot, FootHack delivers time–locked vibrotactile events, but it layers them onto gradual pneumatic compliance changes, yielding richer and more versatile underfoot cues [3, 67]. In addition, FootHack uses gait-driven pressure accumulation and stores compressed air for later release without an active pump. We do not quantify harvested energy and therefore describe energy harvesting only as a potential future use.

This lightweight and unobtrusive form factor is essential for extended sessions. For continuous data collection, in–the–wild virtual reality experiences, or gait–manipulation studies that require many minutes of natural locomotion, added mass, cabling, or elevated sole structures are primary confounds. Heavy footwear and offboard infrastructure alter stance timing, toe clearance, and path choice, reducing ecological validity, as indicated by treadmill–based evaluations of previous systems [84]. FootHack embeds all electronics and the battery within the insole and uses wireless communication. The present studies do not establish that this integration reduces gait interference or supports extended everyday use.

In summary, FootHack integrates pneumatic compliance control, vibrotactile cue delivery, gait-driven pressure accumulation, and embedded sensing in an untethered insole architecture. This integration provides the common platform evaluated in the following studies. Benefits for extended, everyday, or longitudinal use remain to be established.

3 FootHack Prototype

We present an artifact, a flexible 3D-printed shoe sole that features a pneumatic pressure-chamber system with an array of vibration motors. Besides actuation properties, the prototype also incorporates pressure sensors for each chamber and an IMU to identify movement activity, including the gait cycle. The battery, microcontroller, actuators, and sensors are integrated within the insole, eliminating external hardware and enabling untethered operation. A high fidelity hardware prototype is essential to assure matching conditions across participants and minimizing interferences stemming from clunky hardware prototypes. In this section, we will detail the implementation of our device, aiming to enable a replication by third parties.

3.1 Pneumatic Actuation

Our pneumatic system uses custom air chambers embedded in the midsole. Walking supplies energy that is stored as pneumatic energy in the compressed air, which can later be released for feedback without an active pump. We do not quantify that stored energy or claim demonstrated energy harvesting.

3.1.1 General Working Principle. When the foot strikes the ground, body weight and gait load compress the air inside the pressure chamber. The pressure generated within the chambers can then be regulated by a network of electric valves, which allow the system to draw in air from the outside environment, increase internal pressure, or release excess air when necessary. In this manner, the pneumatic system can dynamically adjust to the user's changing needs. More details are provided in Section 3.8. The pressure within the chambers is redistributed as necessary, delivering localized feedback or cushioning based on the user's movements.

3.1.2 Implementation. The pressure chambers and connecting hoses are made from durable, flexible materials. The chambers are *printed with Ninjatek's "Ninjaflex" filament*, chosen for its flexibility [13, 29, 36]. To enhance structural integrity, the pressure chambers are designed with four outer walls (Fig. 2(a)) and feature ironing on every layer (Fig. 2(b)) to ensure airtight sealing. Additionally, the thin walls within the chambers (Fig. 2(c)) improve printability and minimize excessive bulging under pressure. This structural optimization is illustrated in Fig. 2.

Off-the-shelf silicone hoses and pneumatic TPU hoses are used to connect the air chambers to the valves, ensuring efficient airflow between all components. As shown in Fig. 3

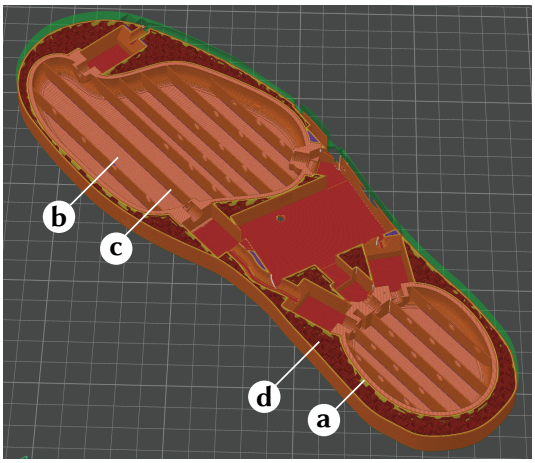


Fig. 2. Sliced 3D-printed prototype of the midsole, showing the internal structure. Orange areas represent layers with ironing applied for a smooth, airtight surface. Dark red regions depict the gyroid infill pattern, optimizing flexibility and cushioning.

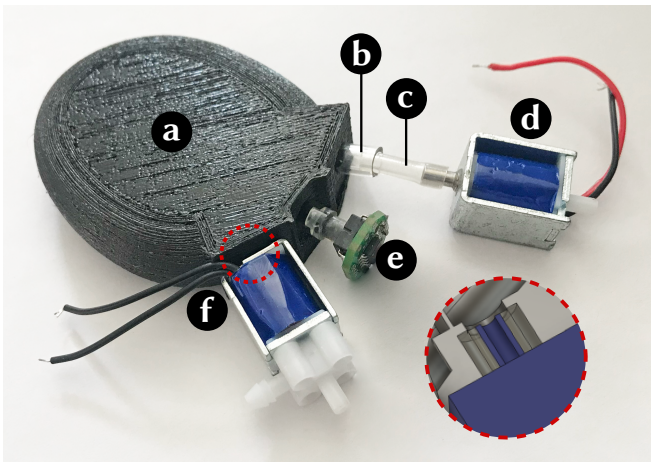


Fig. 3. Displaying the heel part of the air pressure system: a) heel pressure chamber, b) TPU hose, c) silicone hose, d) solenoid valve, e) pressure sensor, and f) final connection.

Technicoll 9310 is a hot-melt adhesive optimized for bonding flexible materials like TPU and metal. Its elasticity and gap-filling properties make it suitable for dynamic applications. In our prototype, it bonds the TPU hose to the 3D-printed structure. The silicone hose (Fig. 3(c)) ensures a tight seal between the valve and sensors (Fig. 3(e)), and also between the valve and the TPU hose (Fig. 3(b)). Additionally, hot glue is used to secure the valve in place.

In Fig. 3(f), the TPU hose (Fig. 3(b)) is shown sealing against an internal 3D-printed stop wall (Fig. 3(a)), while the silicone hose (Fig. 3(c)) acts as a gasket between the valve and the TPU interface.

The pneumatic network uses compact 0520D normally closed solenoid valves from fspump (Fig. 3(d)). The measured current was up to 400 mA at the fully charged battery voltage. Two chamber-to-ambient valves connect the heel and forefoot chambers to ambient, admitting or releasing air according to the pressure gradient, while two opposed connector valves are driven together to exchange air between chambers (Fig. 1(d)). The 3-V valves are driven directly from the 3.0–4.2-V battery only for brief energized intervals. The measured command-to-pressure response and the audible switching limitation are reported in Section 4.

Our pneumatic actuation system relies on precise pressure monitoring. This is achieved using *XGZP6847 A300KPGPN33 analog pressure sensors* embedded in the air chambers. This compound-gauge sensor is itself factory-calibrated and temperature-compensated over −100 to +300 kPa [11]. Its analog output, however, is digitized by the ESP32's built-in analog-to-digital converter, which we did not calibrate as part of the assembled system. We therefore report the raw sensor values used for control and treat any conversion to an absolute pressure as a nominal estimate carrying an unquantified offset (Section 4).

3.2 Vibrotactile Actuation

The vibrational actuation is the second type of feedback the prototype provides. The placement of the vibration motors is guided by pressure points on the foot, as identified in previous research [38, 64]. The top layer of the insole is constructed using Ninjatek's "Chinchilla" filament, chosen for its softness and flexibility, which is further optimized by adjusting the 3D-printing infill density. The material and design ensure that the motors are integrated seamlessly without compromising the user's comfort or the structural integrity of the sole.

3.2.1 Implementation. The *FIT0774 vibration motors* from DFRobot were selected for their compact size and efficiency, making them ideal for integration into the insole. With a diameter of 10 mm and a height of 2.7 mm, these motors are small enough to fit seamlessly into the sole without affecting comfort or mobility. They operate within a voltage range of 1.5V to 4.2V, which aligns with the power supply of the prototype. Despite their compact size, the motors deliver noticeable vibrations to the user. While the PWM signal driving them operates at a frequency of 1500 Hz, the actual vibration frequency of the motors is determined by their mechanical properties and does not directly match the PWM frequency. At full load, they draw only 40 mA. Their low power consumption and compact design make them an ideal choice for the vibration system, ensuring long-term usability while delivering effective haptic feedback. Each coin vibration motor can be driven separately, by the MOSFET Power Stage.

3.2.2 General Working Principle. Our vibrotactile actuation is designed to provide specific feedback patterns, tailored to the user's gait and movement. As demonstrated by Visell et al. [78], vibrations can alter the haptic perception of surfaces. However, unlike their work, which focuses on surface vibrations [77], our approach utilizes an insole-based system for feedback delivery.

3.3 IMU Sensing

The prototype uses an MPU6050 inertial measurement unit with a three-axis accelerometer and three-axis gyroscope, sampled over I2C at 100 Hz. The replaceable breakout-board implementation supports motion sensing, while the pressure channels provide the gait-event signal evaluated in this paper. We do not claim magnetometer-based orientation, stride length, walking speed, or foot-clearance validation.

3.4 Microcontroller

We use an ESP32-S2-MINI-1U-N4 microcontroller [69] with Wi-Fi connectivity and an external antenna connector. Its FreeRTOS runtime schedules sensing, actuation, and background communication, while I2C and SPI support the attached peripherals [68, 70]. The analog pressure channels are used for relative comparisons and sampled at 100 Hz. We do not claim calibrated absolute accuracy for the ESP32 analog readings [59]. Figure 14 shows the component connections.

3.5 Power System

Our prototype is powered by a lithium polymer battery, while other core components include a voltage regulator, and a MOSFET stage to manage the power distribution for the various components, including the ESP32 microcontroller, sensors, valves, and vibration motors.

3.5.1 Battery. The power supply is provided by a Turnigy 1200mAh 1S 1C Li-poly battery pack [56]. This battery was selected due to its compact size, which fits perfectly in the space between the pressure chambers, and its surface area, which is almost identical to that of the PCB components. The 1200 mAh capacity offers sufficient energy storage to meet the power demands of the system during typical usage scenarios. The battery is protected against short circuits, under-voltage, and overcharging, ensuring long-term reliability and safety. The maximum continuous discharge current of the battery is 1200 mA, which is capable of supporting most system loads during operation. In accordance to the datasheet, under maximum theoretical load, the current draw could peak at around 1.6 A for the valves, 200 mA for the vibration motors, 310 mA for the ESP32-S2, 3.7 mA for the MPU6050 gyroscope, and 6 mA for the two pressure sensors, totaling approximately 2119.7 mA. This peak current almost doubles the continuous discharge rating of the battery, which could lead to power limitations under sustained high-load conditions.

3.5.2 Practical Power Consumption. In terms of power consumption, the system is designed in a way that only two valves can be activated simultaneously for a short duration. Additionally, the ESP32 does not transmit continuously, consuming only 30 mA when idle and spiking to 310 mA during transmission. On average, the power consumption for the ESP32 is around 170 mA, with an additional 9.7 mA for the sensors, 100 mA for the vibration motors, and 100 mA for the valves, bringing the total average power consumption to approximately 379.7 mA. This is well within the continuous discharge capacity of the battery, allowing for safe and efficient operation throughout the typical usage period of about 3 hours.

3.5.3 Voltage Regulator. The voltage provided by the lithium polymer battery exceeds the maximum voltage rating of the ESP32, so it needs to be regulated down to 3.3V. Both the gyroscope and air pressure sensor also require a stable voltage between 2.8V and 3.3V to ensure consistent readings when communicating with the ESP32. As the battery discharges, its voltage drops, necessitating a reliable regulator to maintain stability. We use the NCV8187 [53], an LDO (Low Dropout) Linear Voltage Regulator. Specifically, the NCV8187AMT330TAG version is used to maintain a constant 3.3V for the logic system. This chip can handle currents ranging from 1300 to 1750 mA with a dropout voltage of 150 to 220 mV. The ESP32 is designed to shut off at around 2.8V, and the lithium polymer battery at 3.0V, making the regulator ideal for utilizing the full capacity of the battery with its nominal 150 mV voltage drop. The actuators are powered directly from the battery. An oscilloscope capture of the 3.3-V supply during valve switching showed a top-to-base amplitude of approximately 200 mV (300 mV peak-to-peak). This capture characterizes the observed supply-rail waveform; it does not establish the regulator settling time or quantify the effect of switching transients on sensor accuracy.

3.5.4 MOSFET Power Stage. To power the valves and vibration motors, the system relies on a *MOSFET power stage*. The SSM3K7002KFU, LF MOSFET is used due to its ability to handle continuous currents up to 400 mA, with peak pulses reaching 1.2 A. Given the inductive nature of the loads, a freewheeling diode is installed to suppress negative voltage spikes, ensuring the longevity of the components. Additionally, a 680 Ohm resistor and a 10µF capacitor are used to minimize voltage fluctuations, as shown in Figure 14. Protection for the microcontroller is

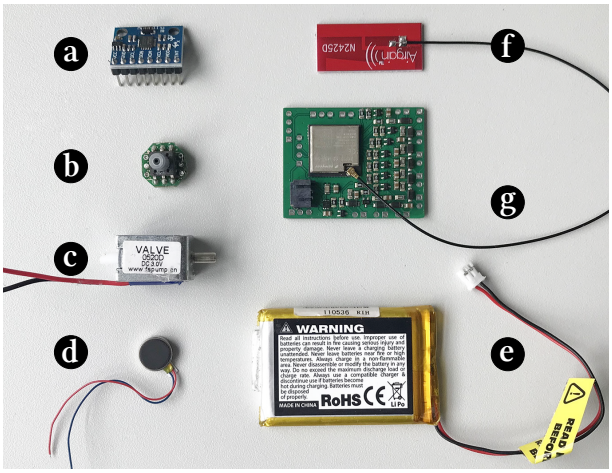


Fig. 4. Prototype hardware: a) IMU, b) Pressure Sensor, c) Solenoid Valve, d) Coin Vibrator, e) Battery, f) Antenna, and g) PCB, with the ESP32 and antenna connector at the center, the MOSFET stages at the top, and the LDO regulator beside the battery connector. Lower-level board and via assignments are provided with the schematic in Appendix A.

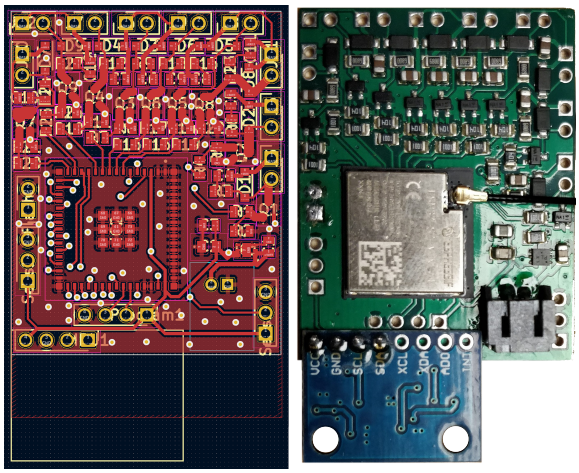


Fig. 5. Prototype PCB showing the front view of the PCB in KiCAD and the actual PCB with all components soldered.

also critical, with a 100 kOhm pull-down resistor and a 1 kOhm limiting resistor in place to restrict current flow to less than 40 mA—well within the safety limits of the ESP32.

The PCB was created in KiCAD, an open source project, which is free of charge. The components and the final PCB can be seen in figure 5. To keep the main text focused on the core method and contribution, the full PCB schematic and lower-level implementation detail are provided in Appendix A.

We chose an off-the-shelf Converse-style shoe as it is easy to modify and provides sufficient user comfort, while saving time for us in producing a durable prototype. We removed the entire sole of the shoe and replaced it with our 3D-printed sole, which consists of an outer sole or shell, a midsole, and an insole. Notably, all components of our system, including the pneumatic actuation, sensors, and vibration motors, are fully contained within the insole itself, requiring no external components. This seamless integration enhances both usability and practicality.

3.6 Shoe

3.6.1 Insole. The top part of the sole that comes into contact with the foot is called the insole. In Fig. 6(a), it consists of two layers: a beige top layer and a thinner black layer underneath, which provides routing space for the cables. These two layers are combined during fabrication. The insole is softer than the rest of the shoe and includes holes for the vibration motors. These motors are glued at the cable exits to prevent cable breakage. We printed the insole using Ninjatek's "Chinchilla" filament, chosen for its high softness and skin comfort.

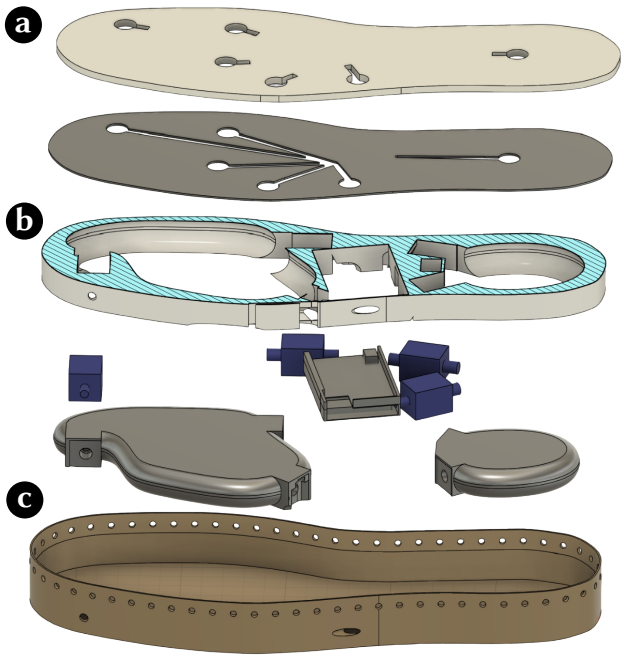


Fig. 6. Explosion image of the Components. a) Insole , b) Midsole, and c) Outsole.

3.6.2 Midsole. The core of the shoe is the midsole, which houses both the pressure chambers and the electronics. In Fig. 6(b), it appears as the light blue and gray sliced part. The darker gray chambers below represent the embedded pressure chambers.

The midsole body is made using Ninjatek's "Chinchilla" TPU, selected for its exceptional softness and elasticity—perfect for wearable applications. This material features an expanding/foaming property and is printed with

a gyroid infill pattern (Fig. 2(d)), which ensures interconnected voids for improved cushioning and eliminates trapped air pockets.

The pressure chambers, in contrast, need to withstand repeated stress and air pressure. Therefore, they are printed from TPU V2 by dasFilament, which offers greater structural strength. To further enhance their durability, we used slicer modifiers to apply additional wall thickness and ironing on every layer, as described in section 3.1.2. This approach ensures the chambers are robust, airtight, and capable of handling dynamic loads during walking. A detailed view of the sliced midsole structure can be seen in Fig. 2.

3.6.3 Outsole. The outsole is the shell and acts as the carrier structure. It securely holds both the midsole and the insole. Additionally, it includes mounting holes to attach it to the fabric that wraps over the top of the foot and around the ankle. This part is more rigid than the other layers and is printed from TPU V2 by dasFilament. In Fig. 6(c), the shell is the brown component at the very bottom of the stack.

All 3D printed parts are designed in Fusion 360, which offers a free educational and hobby license. The STL design files are available in the project repository at https://github.com/susesKaninchen/SimulatingShoe.

3.7 Software

Firmware is implemented as a PlatformIO/Arduino project on the ESP32 FreeRTOS runtime. A high-priority task samples the IMU and two pressure channels at 100 Hz, updates the pneumatic state machine and vibration outputs, and timestamps each record. Network upload and the control web server run in a lower-priority task. Sensing and actuation remain functional without connectivity. Records are buffered in a bounded 400-record FreeRTOS RAM queue. New records are dropped when the queue is full, and buffered records do not survive a reset. Vibration motors use independently controlled 8-bit PWM at 1.5 kHz.

3.8 Actuation Mechanism

The actuation mechanism is twofold, consisting of a pneumatic pressure system that enables a varying softness of the shoe sole and a vibrotactile insole that enables a more obtrusive feedback. The combination of both feedback actuators allows for complex patterns, useful such as to simulate different surface textures one is walking on.

3.8.1 Pneumatic Actuation Principle. To increase pressure in the front chamber, the heel chamber, shown in Figure 1, Section d (blue 2) is compressed by body weight during stance and displaces its air into the larger front chamber, labeled blue 1 in the same figure, when the connecting valves open. Once the pressures equalize, the valves close and the front-chamber pressure is retained. It is crucial that the chambers have different volumes to maintain proper pressure dynamics, allowing the heel chamber to reach higher pressures.

More specifically, when the pressure in either chamber drops below the ambient air pressure by a predefined threshold, the external valve opens, allowing fresh air to enter the system. This mechanism is visualized in the top graph of Figure 8, where the front chamber is intentionally unloaded (i.e., not bearing weight) to isolate and clarify the gradual pressure buildup driven by the heel chamber during the pump-up phase. Once the heel chamber reaches a higher pressure than the front chamber, the internal connecting valves open, enabling air to transfer forward. As soon as the pressures equalize, the valves close, thereby elevating the front chamber's pressure. This cycle repeats until the system reaches the target pressure. At that point, the chambers stabilize just below the desired value, the valves close, and the pressure is maintained. This equalization process is dynamically regulated and synchronized with the gait cycle, as further illustrated in Figure 7.

3.8.2 Simulating Surfaces Textures. To simulate different surfaces, the system combines raw pressure regulation or free inter-chamber exchange with terrain-specific vibration patterns.

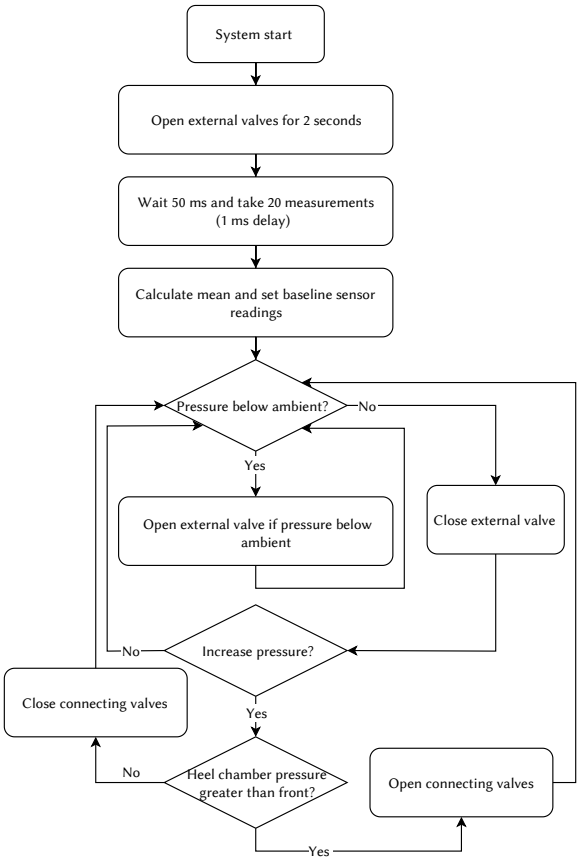


Fig. 7. Flowchart illustrating the pneumatic system's pressure control process. The diagram details initialization, valve operation, and baseline sensor readings, followed by pressure increase logic and equalization. At startup, valves open for 2s before closing; after 50ms, the system averages 20 readings to establish an offset.

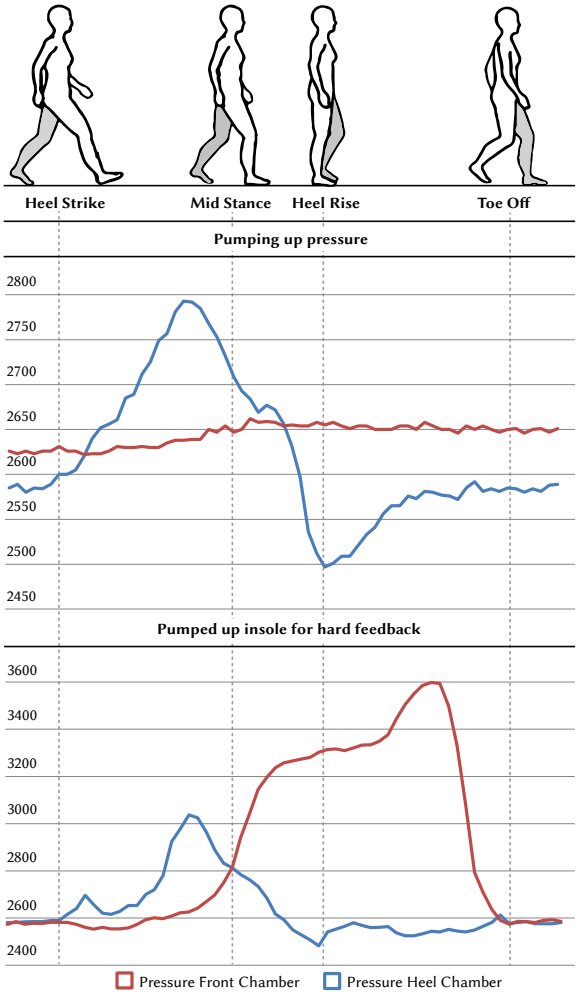


Fig. 8. Pressure profiles across the gait cycle under two system modes. Top: Pressure build-up during the gait-driven build-up phase (front chamber unloaded). Bottom: Pressure evolution during natural walking with pre-inflated chambers, showing typical pressure changes throughout the gait cycle.

The pressure set-points below are raw ADC targets. Table 2 gives nominal, unvalidated gauge-pressure estimates only to convey their approximate scale. For simulating **asphalt**, the pressure target is 3800 (nominally ~61 kPa gauge), with vibrations at nearly full power (PWM of 244) for 50 ms upon ground impact.

For simulating **grass**, the chambers are first preloaded to a raw value of 3000. The inter-chamber valve is then kept open so the front and back chambers exchange air rather than holding that value. This allows the participant to sink into the shoe where more force is applied. The vibration is set to a PWM of 55 whenever the pressure in the front or back increases by more than 60 raw ADC counts above a smoothed baseline value: `baselineH = baselineH * 0.990 + sensorValueH * 0.010`.

For simulating **sand**, the chambers are preloaded to a raw value of 2800 and are likewise kept interconnected afterwards, with no regulated target, while the vibration uses a slightly higher PWM value of 70. Otherwise, it follows the same mechanism as grass, including vibration triggered when the raw reading increases by more than 60 counts.

For simulating **linoleum**, the raw pressure target is 3200 (nominally ~30 kPa gauge), with no vibration and separate chambers.

For simulating **gravel**, the raw pressure target is 3400 (nominally ~41 kPa gauge), with random vibrations occurring upon surface contact at intervals between 0 and 15 ms and PWM values ranging from 0 to 255. Because the vibration motors cannot fully respond to these rapid changes, this results in an average vibration level of approximately 125 PWM.

We selected these configurations in formative pilots to create distinct controller-level combinations intended to be perceptually distinguishable within the controller range already supported by the prototype. The regulated raw targets 3200, 3400, and 3800 provide increasing controller set-points for the three pressure-regulated configurations. They are not psychophysically optimized firmness levels. Linoleum omits vibration to provide a pressure-regulated hard-surface reference, Asphalt combines the highest target with one brief strong impact cue, and Gravel combines an intermediate target with randomized vibration to represent irregularity. Sand and Grass are preloaded once and then keep the chambers interconnected so that no firm target is held, and they use low-amplitude, pressure-change-triggered vibration at two distinct PWM levels. These choices define bundled prototype configurations rather than calibrated physical models of the five terrains.

4 Technical Characterization

Archived recordings describe raw pressure-sensor dynamics, and direct bench measurements characterize valve response, acoustic output, local loading repeatability, apparent pressure retention, gait-driven target build-up, and pressure-derived gait-phase events. The remaining limits of physical pressure calibration and event-threshold calibration are stated explicitly.

Pressure sensing and units. The XGZP6847A300KPGPN33 is a factory-calibrated, temperature-compensated compound-gauge sensor with a specified range of −100 to +300 kPa [11]. The firmware nevertheless acquired it through raw, non-calibrated `analogRead` calls. Archived values above 4095 and their lower-bit pattern are consistent with the ESP32-S2 revision-v0.0 13-bit ADC default and the "ADC-112 bit-1" bug [25, 26]. Startup ambient alignment corrects additive channel offsets only.

Accordingly, raw set-points are our primary control parameters. For the 3.3-V sensor variant, the data-sheet output span of approximately 0.2–2.7 V over −100 to +300 kPa corresponds to a nominal sensitivity of $S = 6.25$ mV/kPa and the transfer function $p_g = (V_{\text{out}} - 0.825\ \text{V})/S$. The historical recordings contain raw ADC codes a, however, not calibrated V_{out}. For scale orientation, we therefore use the observed ambient code $a_0 \approx 2600$

Table 2. System states for the terrain configurations. For the three firm terrains, the front chamber is pressure-regulated to a raw ADC target. For Sand and Grass, the chambers are first brought to the listed raw preload and the inter-chamber valve is then opened, so the chambers exchange air and no target is held while walking. The parenthetical kPa values are nominal, unvalidated gauge-pressure estimates included only for orientation. Exact physical pressures require assembled-system manometer calibration (Section 4). PWM is the 8-bit vibration duty cycle (0–255).

Surface	Chambers	Raw pressure setting	Vibration (PWM)
Asphalt	separate	3800 (~61 kPa nominal gauge)	244, 50 ms on strike
Gravel	separate	3400 (~41 kPa nominal gauge)	0–255 random (avg. 125)
Linoleum	separate	3200 (~30 kPa nominal gauge)	0 (none)
Sand	interconnected	2800 preload, then free exchange	70, triggered by pressure change
Grass	interconnected	3000 preload, then free exchange	55, triggered by pressure change

and the nominal ESP32-S2 13-bit, 11-dB input-span assumption $V_{FS} \approx 2.5$–2.6 V: $\hat{p}_g = (a - a_0)V_{FS}/(8191S)$. This yields the approximate values in Table 2: 61, 41, and 30 kPa gauge for raw targets 3800, 3400, and 3200, respectively. These estimates reconcile the device-native set-points with an approximate physical scale, but are deliberately not presented as measured kPa. The empirical force–ADC response and repeatability measurements below characterize the assembled prototype in the same controller units, while exact physical pressure values would require a manometer calibration.

Dynamic raw-ADC behaviour. The archived on-body logs sampled at 100 Hz contain more than 400 stance events. They show repeated stance-related excursions and gait-driven pressure accumulation without an active pump. They also qualitatively show the intended coupling difference: with the inter-chamber valve open, air redistributes between the heel and front chambers. Regulated modes instead converge toward their raw targets. Because the sensor–ADC chain was not calibrated as an assembled system, we do not convert the archived peaks or per-step changes into physical pressure or energy. Quantifying the stored pneumatic energy would require measuring pressure together with the chamber's change in volume. This was not part of the present study.

Valve response. We performed an exploratory bench characterization under a static preload of 3.7 kg, chosen as a low but reproducible condition that still produced a reliably measurable pressure change. The heel and forefoot chamber-to-ambient paths were each tested over 20 repeated valve commands without timeouts. Median command-to-detectable-pressure-change latency was 6.08 ms at the heel and 10.65 ms at the forefoot (coefficients of variation: 9% and 12%). Separate no-actuation baseline checks for both chambers each completed 20 observation windows without crossing the 30-ADC detection criterion. These values characterize approximate bench response under this preload rather than load-independent actuator constants.

Acoustic characterization. We also performed an orienting acoustic bench characterization with a Google Pixel 9 and dbLogger using A frequency weighting and 35-ms Impulse time weighting. At a controlled distance of 10 cm, the heel, forefoot, and connector valve paths reached L_{AImax} levels of 53.0, 57.8, and 56.9 dB(A), respectively. Three 30-s ambient recordings had a mean L_{Aeq} of 23.1 dB(A). These close-range results confirm that valve actuation is audible and may provide an auditory cue. Because the smartphone microphone was not calibrated against a traceable acoustic calibrator, the absolute levels are orienting estimates and do not establish audibility at the user's ear.

Controlled local loading and repeatability. We characterized both chambers with a fixed local press stamp at 100 mm/min. Five load–unload cycles to a nominal 196 N were performed per chamber, with an ambient-pressure reset between cycles. The press recorded mean cycle peaks of 208.50 ± 1.79 N at the front and 204.27 ± 0.62 N at the heel, reflecting small, repeatable control overshoot. At these measured peaks, the raw-ADC response was highly repeatable (front: mean 3167.6, CV 0.08%; heel: mean 3901.2, CV 0.17%). In the less geometrically constrained 10–50-N portion of three independent loading ramps per chamber, excess ADC counts increased approximately linearly with local force. The mean slopes were 4.58 ± 0.12 ADC/N for the front chamber (mean $R^2 = .998$) and 6.78 ± 0.33 ADC/N for the heel chamber (mean $R^2 = .997$). Progressive stiffening at larger forces indicated increasing geometric constraint by the local stamp rather than a discrete hard-stop transition. Consequently, these measurements characterize repeatability and local force–ADC response in the fixture, not whole-chamber force–pressure calibration.

Apparent pressure retention. In three additional 180-s holds per chamber at nearly fixed press position, the excess raw-ADC response decayed reproducibly. The front and heel chambers reached half of their initial excess after 11.74 ± 0.19 s and 13.29 ± 0.90 s, respectively, and 90% loss after 40.53 ± 0.56 s and 53.49 ± 2.69 s. Descriptive exponential fits yielded time constants of 17.92 ± 0.22 s for the front and 23.12 ± 0.97 s for the heel chamber. Crosshead drift remained below 0.019 mm, while approximately 89–91 N remained at the end of the holds, so the ADC decay was not caused by press unloading alone. These prototype- and fixture-specific retention values combine pneumatic leakage, viscoelastic deformation, and local air-volume redistribution. They are not material leakage constants.

Gait-driven target build-up. We recorded treadmill walking at 3.5 km/h from ambient-aligned chambers with vibration disabled. For each regulated terrain target, three natural-gait repetitions were analyzed from the first detected loading of either chamber (100 raw ADC counts above its run-specific baseline) to the first front-chamber target crossing. Median build-up time was 0.76 s for Linoleum at 3200 (range 0.64–2.10 s), 0.65 s for Gravel at 3400 (0.61–2.05 s), and 16.49 s for Asphalt at 3800 (6.90–23.25 s). Thus, the two lower targets were reached within 2.1 s in every repetition, whereas the highest target was reachable but substantially slower and more variable. One additional Asphalt recording was excluded before summarization because the wearer deliberately applied extra pressure with an abnormal movement after the target was not reached during normal gait. The test path used the deployed controller's pre-target valve logic and commanded chamber equalization immediately after the first crossing. Post-target regulation is therefore outside this analysis.

Objective gait-phase check. A lateral Google Pixel 9 recording at 240 captured frames per second (4.167 ms per frame) was aligned with the 100-Hz serial pressure trace using device timestamps and one shared heel-strike anchor. This alignment event was excluded from the error statistics. Relative pressure-event timing was obtained from the ESP32's monotonic `device_micros` clock rather than laptop USB host-arrival times to avoid serial-buffering jitter. Optical heel strike was defined by the horizontal movement reversal of a colored marker on the instrumented shoe, and optical toe-off as the first frame with a continuous visible gap between the distal sole and treadmill belt, provided that the preceding frame still showed contact. Pressure-derived heel strike was defined by the heel channel exceeding its dynamic baseline by 60 raw ADC counts for three consecutive samples. The pressure-defined unloading event required both pressure channels to remain at or below their respective dynamic baseline plus 60 counts for three consecutive samples.

Across the following 12 gait cycles, all 12 optical heel strikes and all 12 optical toe-offs had one-to-one pressure-event matches, with no accepted missed or additional events. Pressure-derived heel strike showed a mean absolute temporal error of 29.4 ms (median 18.8 ms; maximum 90.8 ms) and occurred 21.3 ms later than the optical event on average. The pressure-defined unloading event was likewise repeatable but preceded optical toe-off by 121.7 ms on average (median absolute error 122.5 ms; maximum absolute error 145.8 ms). Consequently, pressure-derived stance duration averaged 0.653 s (range 0.590–0.690 s), compared with 0.795 s optically (0.754–0.808 s), and was shorter by 143.0 ms on average. The 4.167-ms video frame interval is substantially smaller than this systematic unloading difference. These results support reliable real-time gait-phase detection in this one-wearer, one-speed pilot, while showing that the unloading threshold requires calibration before pressure-derived stance duration can be interpreted as exact optical contact time.

4.1 Ethics, Consent, and Safety

All studies reported in this paper (including the pilot) were conducted within a research program "Cyber-Foot" on foot-based sensing and actuation that was reviewed by the independent ethics committee of the Technical University of Applied Sciences Lübeck, Germany. No ethical concerns were raised, and the approval was issued on 18 January 2022. Before each study, participants were informed about the procedure, the prototype, the data collected, and their right to withdraw at any time without giving reasons. Informed consent was obtained from every participant. Following the approved protocol, we excluded volunteers with gait disabilities, limited leg function, motor or cognitive impairments, and anyone unable to walk more than 100 m. For extended participation, subjects were compensated with a voucher. All collected data were pseudonymised, stored on access-restricted institutional infrastructure, and are retained according to the approved data-management plan before deletion.

Safety. At no point were participants placed in situations hazardous to their health. In Study 2, in which participants walked blindfolded while wearing noise-cancelling earplugs, trials took place on an even, obstacle-free indoor track. Two experimenters were present, and one walked beside the participant to intervene if necessary.

In Study 3, an experimenter was present while participants walked wearing the HMD, and participants could abort at any time.

Data and code availability. Pseudonymised trial data for the three studies, numerical pilot data, and analysis scripts are available at https://github.com/susesKaninchen/FootHack-data. The repository also contains a restricted numerical questionnaire export and numerical bench traces with documentation of their coverage. Direct identifiers, demographic and free-text questionnaire responses, and participant media are excluded. A reproduction command verifies data checksums and regenerates the study analyses; the documentation distinguishes reproducible analyses from bench measurements supplied as data only.

5 Study 1: Perception Properties with Pneumatics & Vibration

Our first physio-psychological study regards the following question (RQ1): *"What are the reaction properties when deploying vibration and pneumatic feedback under the foot?"* Although Anlauf et al. [3] studied a similar aspect with vibrational feedback under the foot, they did not compare it to pneumatic feedback. To close this research gap, we established three hypotheses, which are:

H1: The reaction time when perceiving tactile stimuli at the foot is similar to that of a visual stimulus.
H2: Vibrotactile feedback is better noticeable than pneumatic feedback either by inflation or deflation.
H3: The reaction time is generally enlarged by increased sound levels.

5.1 Study Design

Apparatus: Participants wore both prototype shoes. We used the pneumatic chambers and vibration motors, but not the pressure sensors. The study software triggered each stimulus and stored its timestamp together with a network-latency ping. Inflation increased the pressure in the front chamber, whereas deflation opened the valves and released air to the environment. The system could also equalize the two chambers or return them to ambient pressure. Participants wore a Meta Quest Pro headset and headphones. A stationary camera recorded their responses for later analysis.

Procedure and Task: Participants first completed an eye-to-hand reaction-time test using an online tool[1]. We then fitted the prototype shoes and performed a function check. After entering the VR scene, participants were asked about discomfort such as cybersickness or dizziness. Their task was: *"Move to the VR corridor and raise your arm. Once you feel some type of change under your foot, please make a fist."* The fist indicated whether and when the stimulus had been detected. We tested 12 combinations: inflation, deflation, vibration onset, and vibration offset, each under quiet, soothing-music, and high-noise conditions. The four stimuli were randomized and counterbalanced; the sound levels were not. The recorded dataset contains 325 trials from nine participants: 288 valid reaction-time responses and 37 missed responses. Reaction-time analyses use the 288 valid responses; the miss analysis uses all 325 trials.

Participants: Nine participants (eight male and one female), aged 20–25 years, took part. Participants reported no known sensorimotor impairment and wore EU shoe sizes 39–44.

Data Gathering: Reaction time was measured from the stimulus trigger to the first video frame in which the participant began to make a fist. We subtracted half of the measured round-trip network latency. The camera contributed at most two frames of timing uncertainty, or approximately 33 ms. The remaining one-way network-latency uncertainty was below 5 ms and was small relative to the observed reaction times. We recorded whether each stimulus was detected. An uncertain or missing response was retained as a miss. When such a trial was repeated, the repeat was stored as an additional trial; this explains why trial counts differ between participants. After the session, participants completed a short questionnaire about the session, equipment, and their response behaviour; eight participants responded.

[1] https://humanbenchmark.com

Table 3. Reaction times and miss rates for all Study 1 conditions. Means and standard deviations are calculated from the available participant-level means (n = 8–9). Reaction times include valid responses only. The miss rate is the proportion of trials without a detected response.

	eye-hand		**foot-hand**							
	visual		**inflation**		**deflation**		**vibration on**		**vibration off**	
	M	*SD*	*M*	*SD*	*M*	*SD*	*M*	*SD*	*M*	*SD*
quiet [ms]	252.33	30.72	908.73	246.04	857.88	264.68	745.92	317.42	592.03	108.63
soothing music [ms]	257.56	17.34	957.70	199.48	989.25	167.82	781.84	160.04	817.17	159.42
loud noise [ms]	282.33	36.38	1124.74	282.15	1186.57	393.85	976.76	290.21	1018.24	237.55
across noise lvls [ms]	264.07	23.72	997.05	170.89	1011.23	210.27	834.84	197.78	809.15	109.81
miss rate [%]	0.00	0.00	36.49	20.16	4.29	6.55	1.04	2.95	11.81	13.99

Statistical analysis. We used a separate analysis for each hypothesis. For H1, we compared the quiet visual condition with the four quiet tactile conditions using a repeated-measures ANOVA on the eight complete cases. For H2, we retained the trial-level data. A linear mixed-effects model fitted by restricted maximum likelihood analyzed the 288 valid reaction times. It included participant-specific intercepts and pneumatic-versus-vibrotactile modality slopes. A participant-clustered binomial generalized estimating-equation model with a logit link and exchangeable working correlation analyzed misses across all 325 trials. Both H2 models included stimulus and sound condition. For H3, we used a repeated-measures ANOVA across the three sound conditions and additional stimulus-specific repeated-measures ANOVAs. Given the small sample, we conservatively report Greenhouse–Geisser-corrected results for the H1 and H3 repeated-measures ANOVAs. Focused pairwise comparisons used Holm-Bonferroni correction. We report effect estimates, 95% confidence intervals, and participant-level effect sizes where applicable. No missing reaction time was imputed.

5.2 Results

Table 3 summarizes reaction times and miss rates for all twelve conditions. Prior work reports an average visual reaction time of approximately 250 ms, although age, attention, fatigue, and practice can affect it [37]. Our quiet visual condition was similar (M=252.33 ms, SD=30.72 ms). The displayed means and standard deviations use all available participant means (n = 8–9), whereas the inferential analysis uses the eight complete cases.

The H1 repeated-measures ANOVA showed a condition effect (n = 8, ϵ_{GG} = .70, $F_{2.78,19.48}$ = 13.05, $p < .001$, partial η^2 = .65). All four Holm-Bonferroni-corrected comparisons were significant. Relative to the visual condition, responses were slower for inflation (M=908.73 ms, SD=246.04 ms; Δ = 687.11 ms, 95% CI [481.91, 892.31], $p < .001$, d_z = 2.80), deflation (M=857.88 ms, SD=264.68 ms; Δ = 584.08 ms, 95% CI [356.82, 811.33], p = .001, d_z = 2.15), vibration onset (M=745.92 ms, SD=317.42 ms; Δ = 494.04 ms, 95% CI [252.44, 735.64], p = .002, d_z = 1.71), and vibration offset (M=592.03 ms, SD=108.63 ms; Δ = 340.16 ms, 95% CI [257.98, 422.33], $p < .001$, d_z = 3.46). We therefore **reject H1**: in this task, all tactile conditions produced slower responses than the visual condition.

Prior work shows that vibrotactile feedback is noticeable at other body parts, such as the hand [62]. We assessed noticeability using reaction time and the probability of missing a stimulus. Estimated means were equally averaged across quiet, soothing-music, and high-noise conditions. A joint Wald test of the three stimulus coefficients showed an overall stimulus effect ($\chi^2(3)$ = 10.56, p = .014). The estimated reaction time was 820.57 ms for the combined vibrotactile conditions (95% CI [723.14, 918.00]), 962.05 ms for inflation (95% CI [855.88, 1068.22]), and 1034.02 ms for deflation (95% CI [943.06, 1124.99]).

Both prespecified Holm-Bonferroni-corrected reaction-time comparisons supported H2. Combined vibrotactile feedback was detected faster than inflation (Δ = 141.48 ms, 95% CI [0.21, 282.74], p = .0496) and deflation (Δ = 213.46 ms, 95% CI [83.48, 343.43], p = .0026). The inflation comparison is close to the significance threshold and should be interpreted cautiously.

The participant-clustered binomial generalized estimating-equation model showed the same overall pattern for missed stimuli. A Wald contrast from this model estimated a miss probability of 17.71% for the combined pneumatic conditions and 5.71% for the combined vibrotactile conditions. The difference was 12.00 percentage points (95% CI [5.49, 18.52], $z = 3.61$, $p < .001$). This difference was mainly driven by inflation. Vibrotactile feedback was missed less often than inflation, but its miss probability did not differ from deflation ($p = .572$). Because both reaction-time comparisons supported faster vibrotactile detection and the pooled miss analysis supported the same overall modality advantage, we **accept H2**.

High noise can impair attention and reaction time [93]. The repeated-measures ANOVA showed an overall sound-condition effect in the eight complete cases ($\epsilon_{GG} = .63$, $F_{1.26,8.80} = 10.66$, $p = .008$, partial $\eta^2 = .60$). Responses under high noise were slower than under quiet conditions ($\Delta = 276.16$ ms, 95% CI [88.38, 463.94], Holm-Bonferroni $p = .010$, $d_z = 1.23$) and soothing music ($\Delta = 166.73$ ms, 95% CI [71.84, 261.62], Holm-Bonferroni $p = .009$, $d_z = 1.47$).

The stimulus-specific analyses used the available complete cases ($n = 8$–9). Sound condition was not significant for inflation ($F_{1.24,9.94} = 2.50$, Greenhouse–Geisser $p = .143$, Holm-Bonferroni $p = .258$, partial $\eta^2 = .24$), deflation ($F_{1.51,12.10} = 4.08$, $p = .053$, Holm-Bonferroni $p = .159$, partial $\eta^2 = .34$), or vibration onset ($F_{1.42,9.92} = 2.65$, $p = .129$, Holm-Bonferroni $p = .258$, partial $\eta^2 = .27$). Only vibration offset remained significant after Holm-Bonferroni correction across the four tests ($F_{1.25,8.75} = 12.66$, Greenhouse–Geisser $p = .005$, Holm-Bonferroni $p = .019$, partial $\eta^2 = .64$). For vibration offset, high noise was slower than quiet conditions ($\Delta = 426.21$ ms, 95% CI [187.97, 664.45], Holm-Bonferroni $p = .031$, $d_z = 1.50$), but not slower than soothing music (Holm-Bonferroni $p = .408$). We therefore **confirm H3**: high noise increased reaction time overall, although the effect was not significant for every stimulus. The observed differences were larger than those reported by Peon et al. [54].

Participant feedback. Across eight questionnaire responses, all respondents stated that they had enjoyed the session, and the VR scene was the part named most often. Three quarters reported that they had paid attention to their own reaction time and that the headset had not slowed them down, while the group split evenly on whether the visual scene had distracted them and on whether their reaction speed differed across the sound levels. Across the four rating items, the headset was rated the most comfortable component, followed by the ease of use of the equipment, while insole comfort and the realism of the terrain rendered by the insoles alone received the two lowest ratings. The latter item concerns the isolated inflation, deflation and vibration events used here as detection stimuli and is therefore not comparable to the tuned terrain configurations rated in Study 3. Because these are single items answered by eight participants, we summarize them by rank rather than as means. The Supplement contains only the sanitized response table, with direct identifiers removed and pseudonymous response IDs added.

6 Study 2: Manipulating Gait and Biasing Walking Direction

With the power of a shoe that can substantially change its physical properties, we ask the question (RQ2): *How can we manipulate the user's walking physiology by applying haptic feedback under the foot?* Nurse et al. [52] already indicated that gait could be manipulated under certain circumstances.

6.1 Pilot Study

Full-force vibration under the foot may resemble some type of unstable ground, which makes us subconsciously hitting the ground more carefully. To see whether this assumption is true, we establish two hypotheses:

H4: Augmenting vibrotactile feedback under the foot alters gait.
H5: Varying types of vibration patterns do not have an impact.

6.1.1 Study Design.

Apparatus: In this pilot, we used our pair of shoes with vibrational feedback only, by controlling the 6 vibration

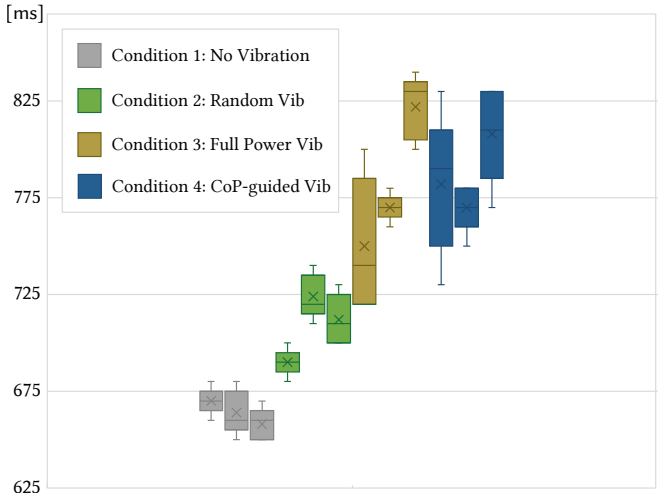


Fig. 9. Stance time for all three participants. No vibration has a lower stance time than random vibration. Full vibration with or without the gait has the largest stance time.

motors. The pressure valve between the air chambers remains closed, so there is no air exchange between both chambers.

Procedure and Task: The procedure starts with an explanation of the task to the participant, after which informed consent was collected (cf. Section 4.1). The prototype was put on and a few steps were walked, so we can assure the functioning of the prototype. The participant then performed the task in four conditions, which are (1) no vibration, (2) random vibration, (3) full vibration, and (4) vibration mapped on Center of Pressure (CoP). Each participant was asked to walk straight down a linoleum floor, for 20 meters, with a turnaround included (walking the same path back to the start). The vibration was presented at both feet.

Participants: We invited three healthy participants, (1m/2f) that had a shoe size of 39, 40, and 42, which fitted into our prototype.

Data Gathering: The chambers were initially brought to a medium preload (in the prototype's raw pressure-sensor units) using pressure accumulated from the participant's own gait rather than an active pump. We estimated stance intervals from the heel and forefoot pressure channels using a threshold approach, while the IMU recorded at 100 Hz as backup. The independent video comparison in Section 4 confirmed one-to-one detection of heel strikes and pressure-defined unloading events in a separate treadmill pilot. However, because unloading occurred systematically before optical toe-off, the reported stance durations are threshold-derived estimates rather than exact optical contact times.

Results: We had a look at several gait parameters, which are: ground reaction force, stance time, and center of pressure. The interesting data, however, provided the stance time, which can be seen in figure 9. It shows the averaged stance time [in milliseconds] over a window of five steps for all three participants. The stance time without any stimulation is usually around M=664 ms (SD=9.86ms) long. With random vibration strength, changing every 10ms, which is nearly equal to half of the possible vibration strength, the stance time is increased to M=708.67ms (SD=17.67ms). The full vibration of the motors enlarged the stance time to M=780.67ms (SD=37.69ms). A CoP-guided vibration, when the user's foot touches the ground, increases stance time similarly to M=786.67ms (SD=29.44ms). These means and standard deviations pool the five-step windows of all three participants, while the hypothesis tests use the participant-level condition means. A one-way repeated-measures ANOVA over those means revealed a significant effect of vibration condition on stance time (ϵ_{GG} = .54; $F_{1.62,3.24}$=23.55; p=.012; partial η^2 = .92), and stance time exceeded each participant's own no-vibration baseline in every vibration

condition. Three Holm-Bonferroni-corrected paired contrasts against that baseline (no vibration) showed CoP-guided vibration to result in significantly longer stance time ($\Delta = 122.67$ms, 95% CI $[63.39, 181.94]$, $t(2) = 8.90$, $p = .037$, $d_z = 5.14$). The increases for full vibration ($\Delta = 116.67$ms, $d_z = 2.71$) and random vibration ($\Delta = 44.67$ms, $d_z = 2.07$) did not reach the conventional significance threshold after Holm-Bonferroni correction (both $p = .085$), although both were directionally consistent with the hypothesized increase. Therefore, we **confirm H4**, solely augmenting vibrotactile feedback under the foot can already significantly alter gait.

Restricting the same participant-level analysis to the three vibration patterns showed that the pattern itself also mattered ($\epsilon_{GG} = .86$; $F_{1.71,3.42}$=13.79; p=.024; partial $\eta^2 = .87$). Behind that effect lies a consistent ordering: random vibration produced the smallest increase, while full power and CoP-guided vibration were nearly indistinguishable from each other ($\Delta = 6.00$ms, $d_z = 0.25$). With three participants none of the individual pattern-to-pattern contrasts survived Holm-Bonferroni correction, so the pattern effect rests on the omnibus test and on that consistent ordering. Therefore, we **reject H5**, the type of vibration has an impact on gait.

6.2 Experiment

As vibration significantly altered stance time in the pilot, the main experiment tested whether asymmetric vibration and cushioning also bias the direction in which the user walks. We hypothesized:

H6: As actuation increases stance time, actuating on only one side will make the user turning to the opposite side when blindfolded.

H7: The combination of vibration and cushioning has the greatest effect in steering the user.

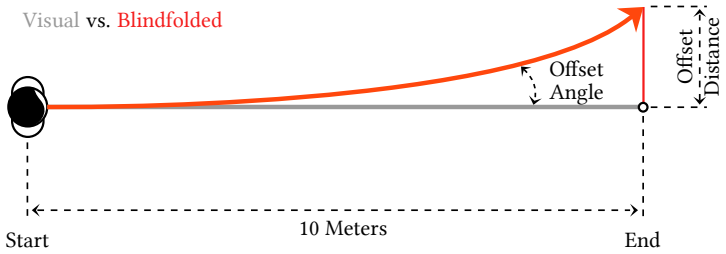


Fig. 10. Schematic drawing that illustrates the experiment and the walking deviation from the center when blindfolded.

6.2.1 *Study Design.*

Apparatus: The prototype pair of shoes was used. In this study, the apparatus varied vibration and raised or lowered chamber pressure by valve switching, using air stored from the participant's gait. An RGB camera was used to record the user.

Procedure and Task: We tested nine conditions: a no-actuation baseline and eight different combinations of actuation (see Table 4). For each condition, the participant was asked to perform 5 trials of walking, whereby each trial is comprised of a 10 m long track. Every participant first completed the five baseline trials – blindfolded and wearing earplugs, but without any actuation – capturing the participant's natural drift when deprived of

Table 4. The eight actuation conditions. L/R denote the left/right foot, V denotes continuous full-intensity vibration, and C denotes pneumatic cushioning reduction through chamber inflation. LV&C and RV&C combine both modalities on the same foot. LV&RC and RV&LC place vibration and cushioning on opposite feet. The separate no-actuation condition provides the participant-specific baseline.

Condition	**1 (LV)**		**2 (LC)**		**3 (LV&C)**		**4 (LV&RC)**		**5 (RV)**		**6 (RC)**		**7 (RV&C)**		**8 (RV&LC)**	
Foot	left	right	left	right	left	right	left	right	left	right	left	right	left	right	left	right
Vibration	x				x		x			x				x		x
Cushioning			x		x			x				x		x	x	

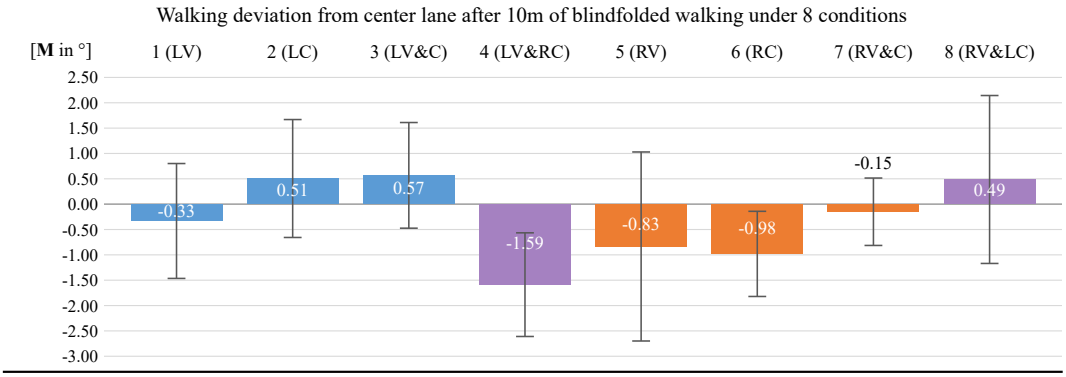
visual and auditory correction. All reported offset angles are computed *relative* to this individual baseline. Due to a scheduling oversight, three participants did not complete the conditions RV, RV&C, and RV&LC (one of them additionally LV&RC), which we report transparently as unbalanced cells rather than dropping the affected conditions. The eight actuation conditions compare vibration and cushioning on the left or right foot, alone and in combination. They are discrete exploratory settings. The study did not test a continuously adjustable steering controller.

The participant started in the middle of the track and mostly ended up with a deviating offset to the center, which was measured (Figure 10). Participants wore noise canceling earplugs and were blindfolded, as in particular the visual sense corrects gait asymmetries, enabling people with gait disabilities, such as leg length discrepancy, to still walk a straight line. The camera was placed behind the start point and the start and end of the recording was controlled remotely by a remote button.

Participants: We invited 9 participants (8m/1f) which were aged between 20-25 years. Experiment inclusion criteria was a shoe size of EU 39-44 and no known gait disabilities.

Data Gathering: In this experiment, we rely on both, quantitative data from the camera. As stated, we also measured the deviation that the participant deviated from the center of the starting point after 10 m of walking. The angle between the center line and the target direction is what we denote as baseline-corrected offset angle. It is the parameter that shows the degree of offset of the participant's walking trajectory. The arrival position was read from the center lane after crossing the finish line. A ruler was used to measure the deviation (see Fig. 10). The offset angle is the arctangent of the deviation from that center over the 10 m track length. Positions were recorded to the nearest 0.5 cm, which corresponds to about 0.03° over 10 m, so the readout is far finer than the effects reported below and the dominant source of variability is the walking behaviour itself. All angles are therefore reported relative to each participant's own no-actuation baseline.

6.2.2 Results. Each participant-condition block comprises five 10 m walks. We summarize every block by a trimmed mean: the largest and the smallest walk are discarded and the remaining three are averaged, so 213 of the 355 recorded walks enter the reported means. Blindfolded walking without visual or auditory correction



	1 (LV)	2 (LC)	3 (LV&C)	4 (LV&RC)	5 (RV)	6 (RC)	7 (RV&C)	8 (RV&LC)
SD in °	1.47	1.51	1.36	1.22	1.78	1.09	0.63	1.58
d_z	-0.23	+0.33	+0.42	-1.30	-0.47	-0.90	-0.24	+0.31
p (Holm)	1	1	1	.064	1	.191	1	1
n	9	9	9	8	6	9	6	6

Fig. 11. Mean baseline-corrected offset angle by actuation condition after 10 m of blindfolded walking. Positive and negative bars indicate opposite drift directions. LV&RC had the largest leftward mean. Error bars are unadjusted 95% confidence intervals of the mean. The table reports standard deviations, Cohen's d_z, Holm-Bonferroni-corrected one-sample p-values, and the available participant count for each condition.

occasionally produces a single extreme walk that would dominate an untrimmed five-walk mean, and the trimmed mean is a standard robust estimator of central tendency for blocks this small. The identical rule is applied to all 71 blocks, including each participant's no-actuation baseline, so it cannot shift the actuation conditions relative to one another or relative to the baseline. This uniform trimming rule defines the descriptive block summaries used in the analysis. The primary mixed-effects model operates on these per-condition means.

As our primary source of information, we determined the dependent variable to be the baseline-corrected offset angle from the center that the user deviated. A positive angle indicates a shift to the right, while a negative angle indicates a shift to the left. The results, displayed in Figure 11, show the gathered data.

Hypothesis tests use the available participant-level data (overall n=9; test-specific n=6–9), with Holm-Bonferroni correction, effect sizes, and 95% confidence intervals. The random-intercept mixed-effects model is the choice for the H6 analysis in conjunction with a complete-case paired testing for sensitivity analysis.

We can form two directional clusters. In the first cluster (blue; Conditions 1, 2, and 3), vibration, cushioning, or both were applied on the left side and were expected to bias walking toward the right. In the second cluster (orange; Conditions 5, 6, and 7), the corresponding right-side configurations were expected to bias walking toward the left. The primary equal-weight contrast in a random-intercept linear mixed model showed a significant contralateral difference ($b = 0.79°$, 95% CI $[0.19, 1.39]$, $z = 2.60$, $p = .009$). The model also showed an overall condition effect (likelihood-ratio $\chi^2(7) = 26.27$, $p < .001$; marginal $R^2 = .26$, conditional $R^2 = .52$). A secondary complete-case paired sensitivity analysis on six participants pointed in the same direction but was not significant (left cluster $M = 0.05°$, right cluster $M = -0.78°$; $M_{diff} = 0.83°$, 95% CI $[-0.35, 2.00]$; $t(5) = 1.80$, $p = .131$, $d_z = 0.74$). We therefore **accept H6** on the basis of the primary mixed-effects contrast across all nine participants with unbalanced condition cells ($n = 6$–9). The six-participant complete-case sensitivity analysis points in the same direction but does not provide statistically significant support ($p = .131$). The primary result indicates a tendency to walk toward the side opposite the actuation. This cluster-level difference was small in absolute terms, below one degree on average over a 10 m walk. It does not imply that every individual condition shifted walking in its expected direction. Stance time was not recorded separately for each foot in this experiment, so the stance-time account of the bias rests on the pilot rather than on a within-experiment measurement.

LV&RC had the largest leftward sample mean (M=−1.59°, 95% CI $[-2.61, -0.56]$; d_z= − 1.30). LV&RC and RC were the two conditions whose unadjusted 95% confidence intervals excluded zero. Neither one-sample test survived Holm-Bonferroni correction across the eight conditions (LV&RC: $p = .064$; RC: $p = .192$). In the H6 mixed-effects model over participant-condition means, LV&RC was lower than the left-cushioning reference by $b = -2.02°$ (95% CI $[-3.00, -1.05]$, $p < .001$). Because LC is not an H7 component condition, this contrast is not a test of H7. In the focused post-hoc family comparing LV&RC against its components, its baseline-corrected offset was more leftward than for left vibration alone ($M_{diff} = -1.17°$, 95% CI $[-1.74, -0.60]$; $t(7) = -4.87$; Holm-Bonferroni-corrected $p = .004$; d_z= − 1.72), but not demonstrably more leftward than for right cushioning alone ($M_{diff} = -0.53°$, 95% CI $[-1.24, 0.18]$; $t(7) = -1.76$; Holm-Bonferroni-corrected $p = .121$; d_z= − 0.62). These two conditions (LV&RC and RV&LC) are especially interesting, because the user perceives different types of feedback on either side. To fully understand this phenomenon, further studies are needed. For now, we **neither accept nor reject H7**. This is a directional bias rather than remote control of the walker. Visual redirected walking remains the established steering approach [50]. The sub-degree offsets observed here indicate only a small complementary directional cue. Because steering and terrain rendering use the same actuators, their combined use remains future work rather than a validated steering system.

7 Study 3: Creating Illusory Terrains

This study is inspired by Wang et al. [84], aiming to create the illusion of different terrains to enrich mixed and virtual reality environments. Compared to previous works using CAVE-like installations [15], our approach is

different, as we use an Oculus Quest [46] and 360° videos recordings. To answer our question (RQ3): *How can we create the illusion of different terrains to enrich virtual reality environments?*, we established two final hypotheses:

H8: It is possible to create a fairly realistic illusion of terrains.
H9: There is no difference between simulating soft and hard surfaces in terms of perceived realism.

7.1 Study Design

Apparatus Next to our shoe prototype, we use a VR-Headset — Oculus Quest [46] showing self-produced 360° videos (Figure 12). The prototype used the five terrain configurations listed in Table 2. These settings were selected in formative pilots and were not calibrated to the mechanical properties of the corresponding physical terrains.

Procedure and Task. The participant was introduced to the study details, the prototype, and the HMD. All trials took place on the same physical linoleum floor while the HMD presented the virtual terrains. The five terrain conditions were presented in randomized order. For each condition, participants took two steps in place with the corresponding controller settings before walking through the scene. This preparation allowed gait-driven pressure accumulation but did not verify that the pressure target had been reached. In the separate bench characterization, the Asphalt target of 3800 required 6.90–23.25 s of walking (Section 4), so it was likely not yet reached at the start of the rated walk after two steps. Target attainment during the rated walk was not verified. Asphalt ratings therefore describe the experienced configuration, potentially including pressure build-up, rather than a verified steady-target condition. For two participants, affected terrain trials were repeated after the researchers noticed that vibration had inadvertently been disabled. The retained matrix contains one documented realism rating per participant and terrain.

Participants: We invited 20 healthy participants aged 22–54 years (10m/10f) with an EU shoe size of 38–42.

Data Gathering: We used two questions after the terrain experiences: (1) *How realistic was the terrain on an 11-pnt Likert scale between 1 to 11?* and (2) *Can you elaborate on your experience?* The displayed scale for the first question was anchored at 1 (not realistic) and 11 (fully realistic). The first question yielded the complete 20-participant by five-terrain rating matrix analysed below. The second question is reported by theme in the results.

Statistical Analysis. We analysed the 11-point Likert-type ratings with parametric statistics because the response scale has at least five ordered levels and the sample-level summaries approximate interval properties. Prior empirical and simulation work shows that parametric methods are robust for such data and typically agree with non-parametric tests [4, 27, 48]. Because every participant rated all five terrains, the terrain factor is within-subjects. We therefore report a one-way repeated-measures ANOVA with partial η^2, followed by paired t-tests with Holm-Bonferroni correction, Cohen's d_z, and 95% confidence intervals. H8 is evaluated with a one-sample t-test of participant means against the neutral midpoint of 6. We also evaluate the overall terrain effect with a Friedman test on the complete 20-participant by five-terrain rating matrix.



Fig. 12. Virtual environments presented through 360-degree video recorded with an Insta360 ONE R Twin Edition [72]: sand (left), asphalt (center), and grass (right).

7.2 Results

On the 1–11 scale, realism was highest for Grass (M=8.35, SD=1.23) and Sand (M=8.05, SD=1.15), followed by Gravel (M=7.25, SD=1.89), Asphalt (M=6.45, SD=1.28), and Linoleum (M=5.75, SD=1.62). Figure 13 shows the rating distribution for each terrain. The mean of the four terrain conditions excluding Linoleum was 7.53. Across all five conditions, a one-sample t-test showed that the participant-level means averaged above the neutral midpoint of 6 (M=7.17, SD=0.72, 95% CI [6.83, 7.51]; $t(19) = 7.23$, $p < .001$, $d_z = 1.62$). We therefore **confirm H8**.

Since Mauchly's test did not reject sphericity ($W = .475$, $\chi^2(9) = 12.97$, $p = .166$), a one-way repeated-measures ANOVA is applicable, which showed a significant terrain effect, $F(4, 76) = 11.75$, $p < .001$, partial $\eta^2 = .38$. The Friedman test also showed an overall terrain effect ($\chi^2(4) = 29.65$, $p < .001$, Kendall's $W = .371$; Appendix B). Four Holm-Bonferroni-corrected paired t-tests were significant: Sand–Asphalt, $\Delta = 1.60$, 95% CI [0.85, 2.35], $p = .002$, $d_z = 1.00$; Sand–Linoleum, $\Delta = 2.30$, 95% CI [1.47, 3.13], $p < .001$, $d_z = 1.29$; Grass–Asphalt, $\Delta = 1.90$, 95% CI [1.02, 2.78], $p = .002$, $d_z = 1.01$; and Grass–Linoleum, $\Delta = 2.60$, 95% CI [1.55, 3.65], $p < .001$, $d_z = 1.16$. No other pair survived Holm-Bonferroni correction. Because the soft terrains were rated more realistic than the hard configurations, we **reject H9**. This difference applies to the tested combinations of pneumatic and vibrotactile settings. Linoleum was the only configuration without vibration, so hardness and vibration presence were not independently manipulated; the higher ratings for the soft configurations cannot be attributed to hardness alone. Linoleum was a linoleum-floor, pressure-regulated, no-vibration hard-surface reference, not a no-actuation, ordinary-shoe, or zero-haptics control. These bundled configurations therefore cannot isolate a causal effect of actuation on realism.

Participant feedback. We summarise the recurring themes across the participant responses. Participants generally described soft terrains as soft and hard terrains as hard. Gravel was sometimes described as sandy or uneven, strong vibration as unusual or excessive, and some participants expressed surprise at the range of sensations and particularly at Sand and Grass.

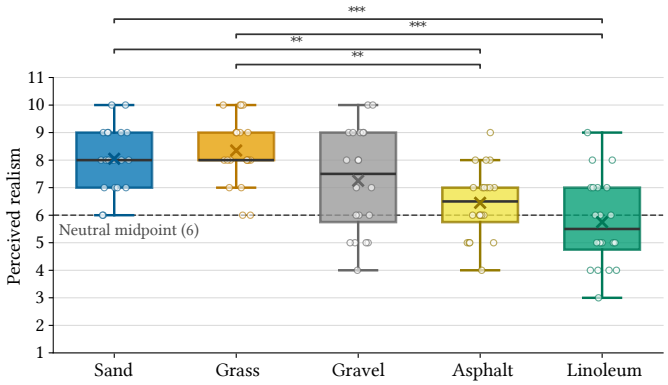


Fig. 13. Perceived terrain realism on the 1–11 scale, where 1 is not realistic and 11 is fully realistic. Grass and Sand received the highest mean ratings. Gravel showed the largest spread (M=7.25, SD=1.89). Linoleum was the linoleum-floor, pressure-regulated, no-vibration hard-surface reference and received the lowest mean rating.

8 Discussion

Generalizability. With our studies, we construct validity as the first stage of internal validity. Generalizability of findings, such as proving external validity in terms of ecological validity, is clearly out of scope here and can, by definition, not be performed by the same researchers to avoid potential bias [9]. Our results should be replicated with different prototypes and with larger sample sizes to confirm external validity. The technical measurements in Section 4 should be repeated across body weights and walking speeds before their results are generalized.

Moreover, our second study with $n = 9$ and the pilot with $n = 3$ may be statistically underpowered, especially given multiple conditions. While we included "no vibration" states, these do not fully substitute a proper 'no-haptics' baseline (e.g., completely inactive insoles), particularly in Study 3 for terrain illusions. Thus, our conclusions should be regarded as indicative tendencies rather than definitive proof. Future work with larger samples, broader demographic coverage, and a fully zero-haptics control condition can help validate and refine these promising results.

The Third Variable Problem. In this research, we did not control for individual differences nor confounding factors such as age, gender, foot size, walking speed, or preference, which may influence the perception or response to foot feedback. There may or may not be a hidden third factor that has a relationship—such as a correlation—to our dependent variables [14]. Within the means of available resources, we tried to carefully design and execute our studies to the best of our knowledge. We followed basic rules, such as always randomizing conditions, running multiple trials, and having a neutral person (other than the experimenter) perform the data analysis. We also note that mechanical artifacts (e.g., audible valve actuation, minor pressure-lag variations) could have drawn participants' attention, influencing results. Furthermore, prior work has at times reported minimal gait effects from vibrotactile insoles in certain populations, suggesting that underlying user characteristics (e.g., neuropathy, mobility level) can be a confounding factor.

Implications. Our findings have several implications for the design of foot-based haptic systems. The findings of Study 1 should be considered when designing vibrotactile information-presentation systems. In future, it should be noted that tactile foot feedback is also negatively impacted by loud noise, since its perception is slower and less sensitive compared to optical stimulation. The findings in Study 2 may be useful when correcting gait issues, such as temporary gait disabilities or functional leg-length discrepancies. However, the observed sub-degree, baseline-corrected offsets require dedicated clinical validation before any such use. Secondly, although blindfolding may seem impractical, wearing an HMD essentially creates the same condition. In HMD-based applications, underfoot cues might complement established visual redirection, but this requires a dedicated combined evaluation. The findings of Study 3 could be implemented in any mixed and virtual reality application to increase immersion and thus user experience. Enhancing running performance with a varying difficulty level in a training scenario is another possible application among many others that may be of interest. Finally, careful design should address potential hardware artifacts (noise, inflation delays) to avoid confounding user perception and to maximize the reliability and reproducibility of foot-based haptic effects.

9 Conclusion

In this paper, we introduced a 3D-printed shoe artifact that is both untethered and unobtrusive. A distinguishing feature is its passive, gait-driven pressure accumulation and storage, which can be utilized to actuate in an energy-efficient way (which is still different than energy harvesting). Alongside the artifact, we contributed three empirical investigations exploring how to "hack" perception at the foot using pneumatic and vibrotactile feedback, guided by three research questions. First, we examined the temporal and sensory limits of foot-based feedback (RQ1). Tactile responses were slower than visual responses, combined vibrotactile feedback was detected faster than inflation and deflation in the tested sample, and high audio-noise increased reaction time overall. Second, we observed a small baseline-corrected association between asymmetric underfoot actuation and walking direction in the tested sample (RQ2). This result establishes a directional bias, not a validated steering nor highly-controlled gait-correction system. Finally, we simulated five terrain conditions, which averaged 7.17 on the 11-point realism scale, supporting the possibility of terrain illusions (RQ3). Together, these findings highlight the physio-psychological characteristics of foot-based feedback and show the feasibility of influencing locomotion and environmental perception through a compact, wearable shoe prototype. Broader causal, clinical, and deployment claims require further evaluation.

Acknowledgment

We thank the participants for their time and contributions to the studies.

References

[1] Muhammad Raheel Afzal, Hosu Lee, Jungwon Yoon, Min-Kyun Oh, and Chang-Han Lee. 2017. Development of an augmented feedback system for training of gait improvement using vibrotactile cues. In *2017 14th International Conference on Ubiquitous Robots and Ambient Intelligence (URAI)*. 818–823. doi:10.1109/URAI.2017.7992833

[2] Neil Aitken. 2019. Most Used Features of Smartwatches. https://whatphone.com.au/guide/most-used-features-of-smartwatches Section: Apple.

[3] Jan Anlauff, Joyce Fung, and Jeremy R. Cooperstock. 2017. VibeWalk: Foot-based tactons during walking and quiet stance. In *2017 IEEE World Haptics Conference (WHC)*. 647–652. doi:10.1109/WHC.2017.7989977

[4] Tamer Baran. 2021. Comparison of Parametric and Non-Parametric Methods to Analyse the Data Gathered by a Likert-Type Scale. In *Handbook of Research on Applied Data Science and Artificial Intelligence in Business and Industry*, Valentina Chkoniya (Ed.). IGI Global, Hershey, PA, 414–430. doi:10.4018/978-1-7998-6985-6.ch020

[5] Cynthia M Baseman, Seka M Dembure, Nathaniel Swinger, Muni T Bondu, Betsy DiSalvo, and Rosa I Arriaga. 2025. Clinical Standards and Proximate Futures: Participatory Design Futuring of Diabetes Technologies with an Under-Resourced Community. *Proceedings of the ACM on Interactive, Mobile, Wearable and Ubiquitous Technologies* 9, 4 (2025), 1–30.

[6] Kurt Edward Beschorner. 2008. *Development of a computational model for shoe-floor-contaminant friction.* Ph. D. Dissertation. University of Pittsburgh.

[7] Sizhen Bian, Mengxi Liu, Bo Zhou, Paul Lukowicz, and Michele Magno. 2024. Body-area capacitive or electric field sensing for human activity recognition and human-computer interaction: A comprehensive survey. *Proceedings of the ACM on interactive, mobile, wearable and ubiquitous technologies* 8, 1 (2024), 1–49.

[8] Harald Böhm, Claudia Oestreich, Roman Rethwilm, Peter Federolf, Leonhard Döderlein, Albert Fujak, and Chakravarty U Dussa. 2019. Cluster analysis to identify foot motion patterns in children with flexible flatfeet using gait analysis—A statistical approach to detect decompensated pathology? *Gait & Posture* 71 (2019), 151–156.

[9] Marilynn Brewer and William D Crano. 2000. Research design and issues of validity. *Handbook of research methods in social and personality psy.* (2000), 3–16.

[10] Bruce Carse, Barry Meadows, Roy Bowers, and Philip Rowe. 2013. Affordable clinical gait analysis: An assessment of the marker tracking accuracy of a new low-cost optical 3D motion analysis system. *Physiotherapy* 99, 4 (2013), 347–351.

[11] CFSensor. 2024. XGZP6847A Pressure Sensor, Version 2.7. https://cfsensor.com/wp-content/uploads/2022/11/XGZP6847A-Pressure-Sensor-V2.7.pdf. Accessed 2026-07-10.

[12] Harish Chander, Reuben F Burch, Purva Talegaonkar, David Saucier, Tony Luczak, John E Ball, Alana Turner, Sachini NK Kodithuwakku Arachchige, Will Carroll, Brian K Smith, et al. 2020. Wearable stretch sensors for human movement monitoring and fall detection in ergonomics. *International journal of environmental research and public health* 17, 10 (2020), 3554.

[13] Michael Chung, Norbert Radacsi, Colin Robert, Edward D McCarthy, Anthony Callanan, Noel Conlisk, Peter R Hoskins, and Vasileios Koutsos. 2018. On the optimization of low-cost FDM 3D printers for accurate replication of patient-specific abdominal aortic aneurysm geometry. *3D printing in medicine* 4, 1 (2018), 1–10.

[14] Lee J Cronbach and Paul E Meehl. 1955. Construct validity in psychological tests. *Psychological bulletin* 52, 4 (1955), 281.

[15] Carolina Cruz-Neira, Daniel J Sandin, Thomas A DeFanti, Robert V Kenyon, and John C Hart. 1992. The CAVE: audio visual experience automatic virtual environment. *Commun. ACM* 35, 6 (1992), 64–73.

[16] Saad Dastagir. 2022. Why Does A Smartwatch Flashes Green? (It's Effect). https://gorilla-fitnesswatches.com/why-does-a-smartwatch-flashes-green/ Blog.

[17] Peter Deetjen. 2005. *Repetitorium Physiologie.* Elsevier, Urban&FischerVerlag.

[18] Sven Delbeck. 2019. Beinimplantat: Mehr Komfort durch Vollbelastbarkeit. https://www.medica.de/de/News/Interviews/%C3%84ltere_Interviews/Interviews_2019/Blutzuckermessung_Infrarot_statt_invasiv

[19] Abdulmotaleb El Saddik, Mauricio Orozco, Mohamad Eid, and Jongeun Cha. 2011. *Haptics technologies: Bringing touch to multimedia.* Springer.

[20] Don Samitha Elvitigala, Roger Boldu, Suranga Nanayakkara, and Denys JC Matthies. 2022. TickleFoot: Design, Development and Evaluation of a Novel Foot-Tickling Mechanism That Can Evoke Laughter. *ACM Transactions on Computer-Human Interaction* 29, 3 (2022), 1–23.

[21] Don Samitha Elvitigala, Jochen Huber, and Suranga Nanayakkara. 2021. Augmented Foot: A Comprehensive Survey of Augmented Foot Interfaces. In *Augmented Humans Conference 2021*. 228–239.

[22] Don Samitha Elvitigala, Denys JC Matthies, Löic David, Chamod Weerasinghe, and Suranga Nanayakkara. 2019. GymSoles: Improving Squats and Dead-Lifts by Visualizing the User's Center of Pressure. In *Proceedings of the 2019 CHI Conference on Human Factors in Computing Systems*. 1–12.

[23] Don Samitha Elvitigala, Denys JC Matthies, and Suranga Nanayakkara. 2020. StressFoot: Uncovering the potential of the foot for acute stress sensing in sitting posture. *Sensors* 20, 10 (2020), 2882.

[24] Don Samitha Elvitigala, Denys JC Matthies, Chamod Weerasinghe, and Suranga Nanayakkara. 2021. GymSoles++: Combining Google Glass with Smart Insoles to Improve Body Posture when Performing Squats. In *The 14th PErvasive Technologies Related to Assistive Environments Conference*. 48–54.

[25] Espressif Systems. 2026. Analog to Digital Converter (ADC) — Arduino ESP32 Documentation. https://docs.espressif.com/projects/arduino-esp32/en/latest/api/adc.html. Accessed 2026-07-10.

[26] Espressif Systems. 2026. ESP32-S2 Chip Revision v0.0 Errata: ADC-112, SAR ADC Bit 1 Does Not Flip. https://docs.espressif.com/projects/esp-chip-errata/en/latest/esp32s2/03-errata-description/esp32s2/sar-adc-bit1-no-flip.html. Accessed 2026-07-10.

[27] Jacques M. Franc, Kevin K. C. Hung, Andrea Pirisi, and Eitan S. Weinstein. 2023. Analysis of Delphi study 7-point linear scale data by parametric methods: use of the mean and standard deviation. *Methodological Innovations* 16, 2 (2023), 226–233. doi:10.1177/20597991231179393

[28] Yang Gao, Wenbo Zhang, Junbin Ren, Ruihao Zheng, Yingcheng Jin, Di Wu, Lin Shu, Xiangmin Xu, and Zhanpeng Jin. 2024. Pressinpose: Integrating pressure and inertial sensors for full-body pose estimation in activities. *Proceedings of the ACM on Interactive, Mobile, Wearable and Ubiquitous Technologies* 8, 4 (2024), 1–28.

[29] David Garcia, Ziling Wu, Jee Yun Kim, Z Yu Hang, and Yunhui Zhu. 2019. Heterogeneous materials design in additive manufacturing: Model calibration and uncertainty-guided model selection. *Additive Manufacturing* 27 (2019), 61–71.

[30] Rupesh Gupta, Sarang Sharma, Sheifali Gupta, and Deepali Gupta. 2019. Stackable smart footwear rack using infrared sensor. *Journal of Computational and Theoretical Nanoscience* 16, 10 (2019), 4232–4235.

[31] Marian Haescher, Denys JC Matthies, Gerald Bieber, and Bodo Urban. 2015. Capwalk: A capacitive recognition of walking-based activities as a wearable assistive technology. In *Proceedings of the 8th ACM International Conference on PErvasive Technologies Related to Assistive Environments*. 1–8.

[32] Mahmoud Hassan, Florian Daiber, Frederik Wiehr, Felix Kosmalla, and Antonio Krüger. 2017. Footstriker: An EMS-based foot strike assistant for running. *Proceedings of the ACM on Interactive, Mobile, Wearable and Ubiquitous Technologies* 1, 1 (2017), 1–18.

[33] YUKO ICHIKAWA. 2021. Cybershoes for Quest & SteamVRVR Gaming Shoe. https://www.cybershoes.com/us/features/

[34] Frank Imbach, Robin Candau, Romain Chailan, and Stephane Perrey. 2020. Validity of the Stryd Power Meter in Measuring Running Parameters at Submaximal Speeds. *Sports* 8, 7 (2020), 103. doi:10.3390/sports8070103

[35] J. T. Inglis, C. L. Shupert, F. Hlavacka, and F. B. Horak. 1995. Effect of galvanic vestibular stimulation on human postural responses during support surface translations. *Journal of Neurophysiology* 73, 2 (1995), 896–901. arXiv:https://doi.org/10.1152/jn.1995.73.2.896 doi:10.1152/jn.1995.73.2.896 PMID: 7760147.

[36] Alexandra Ion, Robert Kovacs, Oliver S Schneider, Pedro Lopes, and Patrick Baudisch. 2018. Metamaterial textures. In *Proceedings of the 2018 CHI Conference on Human Factors in Computing Systems*. 1–12.

[37] AA Jayaswal. 2016. Comparison between auditory and visual simple reaction times and its relationship with gender in 1st year MBBS students of Jawaharlal Nehru Medical College, Bhagalpur, Bihar. *Int. J. Med. Res. Rev* 4 (2016), 1228–1232.

[38] Wonsun Kim, Woojin Shin, Hyunji Kim, and Hojun Yeom. 2020. Development of Gait Correction System for Real-Time Gait. *International journal of advanced smart convergence* 9, 4 (2020), 139–148.

[39] Rayner Zheng Xian Lee. 2021. An experimental investigation of shape memory sock-shoes. (2021).

[40] Rensis Likert. 1932. *A technique for the measurement of attitudes.* Number 140 in Archives of Psychology. Columbia University, New York, NY, USA. 1–55 pages. https://legacy.voteview.com/pdf/Likert_1932.pdf

[41] Michael Locke. 1984. Epidermal cells. In *Biology of the Integument: Invertebrates*. Springer, 502–522.

[42] Denys J.C. Matthies, Don Samitha Elvitigala, Annis Fu, Deborah Yin, and Suranga Nanayakkara. 2021. mobiLLD: Exploring the Detection of Leg Length Discrepancy and Altering Gait with Mobile Smart Insoles. In *The 14th PErvasive Technologies Related to Assistive Environments Conference (PETRA 2021)*. Association for Computing Machinery, New York, NY, USA, 37–47. doi:10.1145/3453892.3453896

[43] Denys JC Matthies, Franz Müller, Christoph Anthes, and Dieter Kranzlmüller. 2013. ShoeSoleSense: proof of concept for a wearable foot interface for virtual and real environments. In *Proceedings of the 19th ACM Symposium on Virtual Reality Software and Technology*. 93–96.

[44] Denys J. C. Matthies, Thijs Roumen, Arjan Kuijper, and Bodo Urban. 2017. CapSoles: Who is Walking on What Kind of Floor?. In *Proceedings of the 19th International Conference on Human-Computer Interaction with Mobile Devices and Services* (Vienna, Austria) *(MobileHCI '17)*. Association for Computing Machinery, New York, NY, USA, Article 9, 14 pages. doi:10.1145/3098279.3098545

[45] Anita Meier, Denys JC Matthies, Bodo Urban, and Reto Wettach. 2015. Exploring vibrotactile feedback on the body and foot for the purpose of pedestrian navigation. In *Proceedings of the 2nd international Workshop on Sensor-based Activity Recognition and Interaction*. 1–11.

[46] Meta. 2022. Oculus Quest. https://www.meta.com/de/en/quest/products/quest-2/ Page Version ID: 220979159.
[47] Dennis Metz. 2022. Digitsole Smartshoe ist ein selbstschnürender Sneaker. https://www.gadget-rausch.de/digitsole-smartshoe-ist-ein-selbstschnuerender-sneaker/
[48] Jacqueline Murray. 2013. Likert Data: What to Use, Parametric or Non-Parametric? *International Journal of Business and Social Science* 4, 11 (2013), 258–264. https://ijbssnet.com/journals/Vol_4_No_11_September_2013/23.pdf
[49] A Mohamed Nazeer, S Sasikala, M Sathish Kumar, M Yogeshwaran, K Veeramani, and R Vigneshwaran. 2020. Arduino Controlled Cooling Smart Footwear. *International Journal of Scientific Research in Science and Technology* (2020), 327–331. doi:10.32628/IJSRST207480
[50] Niels Christian Nilsson, Tabitha Peck, Gerd Bruder, Edward Hodgson, Stefania Serafin, Mary Whitton, and Frank Steinicke. 2018. 15 Years of Research on Redirected Walking in Immersive Virtual Environments. *IEEE Computer Graphics and Applications* 38, 2 (2018), 44–56. doi:10.1109/MCG.2018.111125628
[51] Jean Bosco Nkurunziza, Ross Brancati, Ramzi Majaj, Jeremy Gummeson, and Michael Busa. 2026. Embedded Smart Insole for Accurate Gait Event Detection. *Proceedings of the ACM on Interactive, Mobile, Wearable and Ubiquitous Technologies* 10, 1 (2026), 1–17.
[52] Matthew A. Nurse, Manuel Hulliger, James M. Wakeling, Benno M. Nigg, and Darren J. Stefanyshyn. 2005. Changing the texture of footwear can alter gait patterns. *Journal of Electromyography and Kinesiology* 15, 5 (2005), 496–506. doi:10.1016/j.jelekin.2004.12.003
[53] onsemi. 2021. Voltage Regulator - Low Iq, Low Dropout, Power Good Output 1.2A NCV8187. https://invensense.tdk.com/wp-content/uploads/2015/02/MPU-6000-Datasheet1.pdf.
[54] Adrian Ramos Peon and Domenico Prattichizzo. 2013. Reaction times to constraint violation in haptics: comparing vibration, visual and audio stimuli. In *2013 world haptics conference (WHC)*. IEEE, 657–661.
[55] Max Pfeiffer, Tim Dünte, Stefan Schneegass, Florian Alt, and Michael Rohs. 2015. Cruise Control for Pedestrians: Controlling Walking Direction using Electrical Muscle Stimulation. In *Proceedings of the 33rd Annual ACM Conference on Human Factors in Computing Systems* (Seoul, Republic of Korea) *(CHI '15)*. Association for Computing Machinery, New York, NY, USA, 2505–2514. doi:10.1145/2702123.2702190
[56] pknergy. 2022. Li-Polymer Battery Technology Specification. https://ecksteinimg.de/Datasheet/ZB07002/LP503562%201200mAH%203.7V%201S1P%20A0.pdf.
[57] Kazi Kowshin Raihana, Md. Sabbir Hossain, Md. Tahsan Dewan, and Hasan U. Zaman. 2018. Auto-Moto Shoes: An Automated Walking Assistance for Arthritis Patients. In *2018 2nd International Conference on Electronics, Materials Engineering & Nano-Technology (IEMENTech)*. 1–8. doi:10.1109/IEMENTECH.2018.8465302
[58] Anil Raj and James Perry. 2000. Vibrotactile Displays for Improving Spatial Awareness. *Proceedings of the Human Factors and Ergonomics Society Annual Meeting* 44 (07 2000). doi:10.1177/154193120004400148
[59] Random Nerd Tutorials. 2019. ESP32 ADC – Read Analog Values with Arduino IDE. https://randomnerdtutorials.com/esp32-adc-analog-read-arduino-ide/
[60] Prabhav Nadipi Reddy, Glen Cooper, Andrew Weightman, Emma Hodson-Tole, and Neil Reeves. 2016. An in-shoe temperature measurement system for studying diabetic foot ulceration etiology: preliminary results with healthy participants. *Procedia cirp* 49 (2016), 153–156.
[61] Junbin Ren, Ruihao Zheng, Wenbo Zhang, Dong She, Yuting Bai, ZhanPeng Jin, and Yang Gao. 2025. Motion2Press: Cross Model Learning from IMU to Plantar Pressure for Gait Analysis. *Proceedings of the ACM on Interactive, Mobile, Wearable and Ubiquitous Technologies* 9, 3 (2025), 1–33.
[62] Thijs Roumen, Simon T Perrault, and Shengdong Zhao. 2015. Notiring: A comparative study of notification channels for wearable interactive rings. In *Proceedings of the 33rd Annual ACM CHI 2015*. 2497–2500.
[63] Dominik Schmidt, Rob Kovacs, Vikram Mehta, Udayan Umapathi, Sven Köhler, Lung-Pan Cheng, and Patrick Baudisch. 2015. Level-Ups: Motorized Stilts that Simulate Stair Steps in Virtual Reality. In *Proceedings of the 33rd Annual ACM Conference on Human Factors in Computing Systems* (Seoul, Republic of Korea) *(CHI '15)*. Association for Computing Machinery, New York, NY, USA, 2157–2160. doi:10.1145/2702123.2702253
[64] Neel Shah, Laxit Kamdar, Drashti Gokalgandhi, and Ninad Mehendale. 2021. Walking pattern analysis using deep learning for energy harvesting smart shoes with IoT. *Neural Computing and Applications* 33, 18 (2021), 11617–11625.
[65] Peter B. Shull, Haisheng Xia, Jesse M. Charlton, and Michael A. Hunt. 2021. Wearable Real-Time Haptic Biofeedback Foot Progression Angle Gait Modification to Assess Short-Term Retention and Cognitive Demand. *IEEE Transactions on Neural Systems and Rehabilitation Engineering* 29 (2021), 1858–1865. doi:10.1109/TNSRE.2021.3110202
[66] Hyungki Son, Hyunjae Gil, Sangkyu Byeon, Sang-Youn Kim, and Jin Ryong Kim. 2018. Realwalk: Feeling ground surfaces while walking in virtual reality. In *Extended Abstracts of the 2018 CHI Conference on Human Factors in Computing Systems*. 1–4.
[67] Paul Strohmeier, Seref Güngör, Luis Herres, Dennis Gudea, Bruno Fruchard, and Jürgen Steimle. 2020. BARefoot: Generating Virtual Materials Using Motion Coupled Vibration in Shoes. In *Proceedings of the 33rd Annual ACM Symposium on User Interface Software and Technology* (Virtual Event, USA) *(UIST '20)*. Association for Computing Machinery, New York, NY, USA, 579–593. doi:10.1145/3379337.3415828
[68] Espressif Systems. 2021. ESP32-S2 Family. https://espressif.com/sites/default/files/documentation/esp32-s2_datasheet_en.pdf.

[69] Espressif Systems. 2021. ESP32S2MINI1 & ESP32S2MINI1. https://www.mouser.de/datasheet/2/891/esp32_s2_mini_1_esp32_s2_mini_1u_datasheet_en-1928084.pdf.

[70] Espressif Systems. 2022. FreeRTOS. https://docs.espressif.com/projects/esp-idf/en/latest/esp32/api-reference/system/freertos.html.

[71] Yuichiro Takeuchi. 2010. Gilded gait: reshaping the urban experience with augmented footsteps. In *Proceedings of the 23nd Annual ACM Symposium on User Interface Software and Technology* (New York, New York, USA) *(UIST '10)*. Association for Computing Machinery, New York, NY, USA, 185–188. doi:10.1145/1866029.1866061

[72] PR Team. 2022. Insta360 ONE R Twin Edition | Duales Objektiv | 360° Panorama | 4K Weitwinkel | FlowState Stabilisierte Action Kamera | Wechselobjektive. https://www.insta360.com/de/product/insta360-oner_twin-edition

[73] Sales team. 2022. Digitsole® digital health company and leader in the e-health space. https://digitsole.com/

[74] Stryd Team. 2022. Running with Power. https://www.stryd.com/us/www.stryd.com/us/en/

[75] Chih-An Tsao, Tzu-Chun Wu, Hsin-Ruey Tsai, Tzu-Yun Wei, Fang-Ying Liao, Sean Chapman, and Bing-Yu Chen. 2022. FrictShoes: Providing Multilevel Nonuniform Friction Feedback on Shoes in VR. *IEEE Transactions on Visualization and Computer Graphics* 28, 5 (2022), 2026–2036. doi:10.1109/TVCG.2022.3150492

[76] Keigo Ushiyama and Pedro Lopes. 2023. FeetThrough: Electrotactile Foot Interface that Preserves Real-World Sensations. In *Proceedings of the 36th Annual ACM Symposium on User Interface Software and Technology* (San Francisco, CA, USA) *(UIST '23)*. Association for Computing Machinery, New York, NY, USA, Article 10, 11 pages. doi:10.1145/3586183.3606808

[77] Yon Visell and Jeremy R. Cooperstock. 2010. Design of a vibrotactile display via a rigid surface. In *2010 IEEE Haptics Symposium*. 133–140. doi:10.1109/HAPTIC.2010.5444664

[78] Yon Visell, Bruno L. Giordano, Guillaume Millet, and Jeremy R. Cooperstock. 2011. Vibration Influences Haptic Perception of Surface Compliance During Walking. *PLOS ONE* 6, 3 (03 2011), 1–11. doi:10.1371/journal.pone.0017697

[79] Cheng Wang, Xiangdong Wang, Zhou Long, Jing Yuan, Yueliang Qian, and Jintao Li. 2016. Estimation of temporal gait parameters using a wearable microphone-sensor-based system. *Sensors* 16, 12 (2016), 2167.

[80] Liang Wang, Wen Cheng, Lijia Pan, Tao Gu, Tianheng Wu, Xianping Tao, and Jian Lu. 2018. Spiderwalk: Circumstance-aware transportation activity detection using a novel contact vibration sensor. *Proceedings of the ACM on Interactive, Mobile, Wearable and Ubiquitous Technologies* 2, 1 (2018), 1–30.

[81] Li-Yang Wang, Ping-Hsuan Han, and Liwei Chan. 2022. Push-Ups: Enhancing Kinesthetic Experience with Shape-Forming Devices on the Feet Soles. In *Proceedings of the Sixteenth International Conference on Tangible, Embedded, and Embodied Interaction* (Daejeon, Republic of Korea) *(TEI '22)*. Association for Computing Machinery, New York, NY, USA, Article 27, 8 pages. doi:10.1145/3490149.3501333

[82] Yue Wang and Mark A Minor. 2014. Design of a bladder based elastomeric Smart Shoe for haptic terrain display. In *2014 IEEE/RSJ International Conference on Intelligent Robots and Systems*. IEEE, 1236–1241.

[83] Yue Wang and Mark A. Minor. 2018. Design and Evaluation of a Soft Robotic Smart Shoe for Haptic Terrain Rendering. *IEEE/ASME Transactions on Mechatronics* 23, 6 (2018), 2974–2979. doi:10.1109/TMECH.2018.2871631

[84] Yue Wang, Takara E. Truong, Samuel W. Chesebrough, Pete Willemsen, K. Bo Foreman, Andrew S. Merryweather, John M. Hollerbach, and Mark A. Minor. 2021. Augmenting Virtual Reality Terrain Display with Smart Shoe Physical Rendering: A Pilot Study. *IEEE Transactions on Haptics* 14, 1 (2021), 174–187.

[85] wiseGEEK. 2022. What Is the Fastest Sense in Humans? http://www.thehealthboard.com/what-is-the-fastest-sense-in-humans.htm

[86] Dennis Wittchen, Valentin Martinez-Missir, Sina Mavali, Nihar Sabnis, Courtney N. Reed, and Paul Strohmeier. 2023. Designing Interactive Shoes for Tactile Augmented Reality. In *Proceedings of the Augmented Humans International Conference 2023* (Glasgow, United Kingdom) *(AHs '23)*. Association for Computing Machinery, New York, NY, USA, 1–14. doi:10.1145/3582700.3582728

[87] Jacob O Wobbrock and Julie A Kientz. 2016. Research contributions in human-computer interaction. *interactions* 23, 3 (2016), 38–44.

[88] Tianhao Wu, Yi Wu, Bibek Poudel, Syed Irfan Ali Meerza, Rajasi Gore Athawale, Weizi Li, Zan Gao, Çağdas KarataŞ, and Jian Liu. 2025. Vibrun: Real-time unobtrusive gait analysis for treadmill running via footstep vibrations. *Proceedings of the ACM on Interactive, Mobile, Wearable and Ubiquitous Technologies* 9, 3 (2025), 1–25.

[89] Haisheng Xia, Jesse M. Charlton, Peter B. Shull, and Michael A. Hunt. 2020. Portable, automated foot progression angle gait modification via a proof-of-concept haptic feedback-sensorized shoe. *Journal of Biomechanics* 107 (2020), 109789. doi:10.1016/j.jbiomech.2020.109789

[90] Jackie (Junrui) Yang, Christian Holz, Eyal Ofek, and Andrew D. Wilson. 2019. DreamWalker: Substituting Real-World Walking Experiences with a Virtual Reality. In *Proceedings of the 32nd Annual ACM Symposium on User Interface Software and Technology* (New Orleans, LA, USA) *(UIST '19)*. Association for Computing Machinery, New York, NY, USA, 1093–1107. doi:10.1145/3332165.3347875

[91] Tuo Yu, Haiming Jin, and Klara Nahrstedt. 2019. Shoesloc: In-shoe force sensor-based indoor walking path tracking. *Proceedings of the ACM on Interactive, Mobile, Wearable and Ubiquitous Technologies* 3, 1 (2019), 1–23.

[92] EC Zeeman. 2006. Morse inequalities for diffeomorphisms with shoes and flows with solenoids. In *Dynamical Systems—Warwick 1974: Proceedings of a Symposium Held at the University of Warwick 1973/74*. Springer, 44–47.

[93] Alireza Zeydabadi, Jafar Askari, Mahmood Vakili, Seyyed Jalil Mirmohammadi, Mohammad Ali Ghovveh, and Amir Houshang Mehrparvar. 2019. The effect of industrial noise exposure on attention, reaction time, and memory. *International archives of occupational and environmental health* 92 (2019), 111–116.

[94] LUO ZHI-FANG. 2009. Espacenet – Suchergebnisse. https://worldwide.espacenet.com/patent/search/family/044994912/publication/TW201038218A?q=TW201038218A

A Supplementary Hardware Details

This appendix provides the PCB schematic and supporting hardware implementation details.

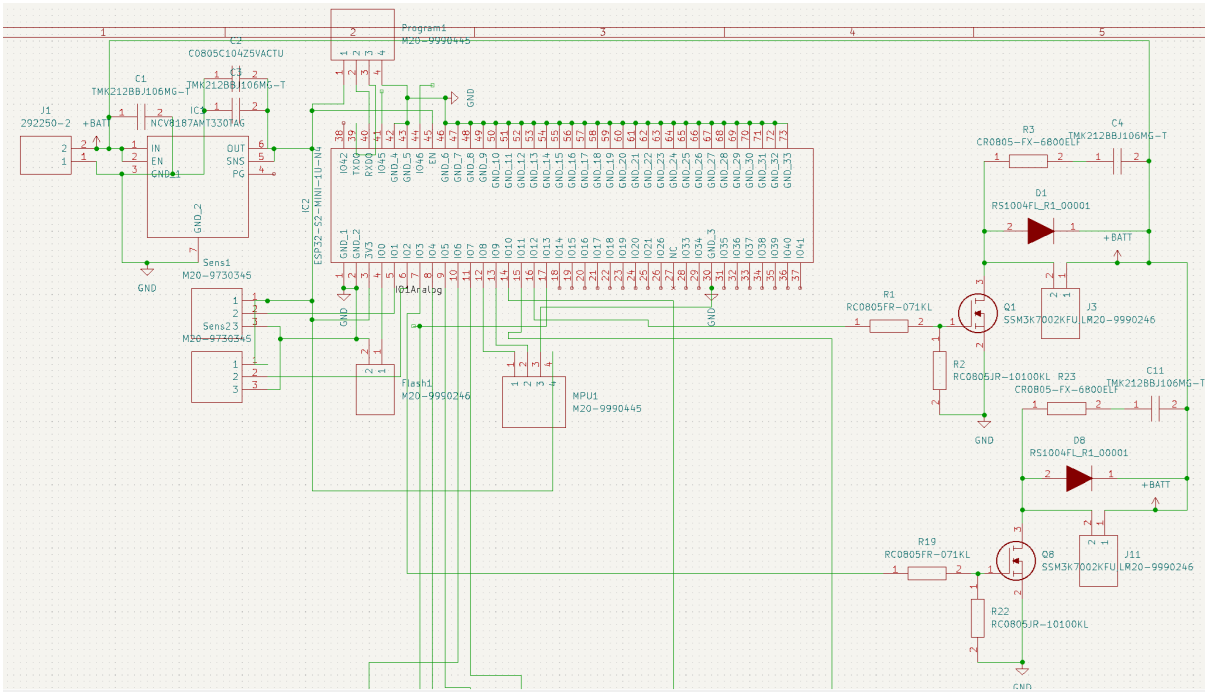


Fig. 14. Schematic of the PCB with an overview of key components. Not all MOSFET stages are shown to provide a clearer view. In the center is the ESP32, with the step-down converter on the left and two MOSFET stages on the right. The remaining boxes represent connectors for external components.

B Supplementary Statistical Analyses

For the **Study 2 gait pilot** (stance time, $n = 3$, within-subjects), a distribution-free Friedman test over the participant-level condition means agreed with the repeated-measures ANOVA ($\chi^2(3) = 8.38$, $p = .039$). The recovered step-level records preserve the same participant-column order across conditions, and the participant-level means were paired in that order.

For **Study 3** ($n = 20$), the Friedman test ranks each participant's five terrain ratings within participant and accounts for tied ranks. It yielded $\chi^2(4) = 29.65$, $p = 5.76 \times 10^{-6}$, and Kendall's $W = \chi^2/[20(5-1)] = .371$. This distribution-free check agrees with the repeated-measures ANOVA on the presence of an overall terrain effect. It does not separately test the pairwise contrasts reported in the main text.